SPICAM on Mars Express: A 10 year in-depth survey of the Martian atmosphere

F. Montmessin[a,*], O. Korablev[b], F. Lefèvre[c], J.-L. Bertaux[a], A. Fedorova[b], A. Trokhimovskiy[b], J.Y. Chaufray[a], G. Lacombe[a], A. Reberac[a], L. Maltagliati[d], Y. Willame[e], S. Guslyakova[b], J.-C. Gérard[f], A. Stiepen[e], D. Fussen[f], N. Mateshvili[f], A. Määttänen[a], F. Forget[g], O. Witasse[h], F. Leblanc[a], A.C. Vandaele[f], E. Marcq[a], B. Sandel[i], B. Gondet[j], N. Schneider[k], M. Chaffin[k], N. Chapron[a]

[a] CNRS LATMOS, Laboratoire Atmosphères, Milieux, Observations Spatiales, Université Versailles St Quentin en Yvelines, Quartier des Garennes, 11 bd d'Alembert, 78280 Guyancourt, France
[b] Space Research Institute, 84/32 Profsoyuznaya St, Moscow, Russia
[c] CNRS LATMOS, Université Pierre et Marie Curie, 4 place Jussieu, 75252 Paris, France
[d] CEA-Saclay, route Nationale, Gif-sur-Yvette, France
[e] BIRA-IASB, avenue Circulaire 3, Brussels, Belgium
[f] LPAP, Université de Liège, Quartier Agora, 19c allée du 6 août, Liège, Belgium
[g] CNRS LMD, 4 place Jussieu, 75252 Paris Cédex, France
[h] ESA-ESTEC, Keplerlaan 1, 2201 AZ Noordwijk, Netherland
[i] LPL, University of Arizona, Tucson, AZ, United States
[j] Institut d'Astrophysique Spatiale, Orsay, France
[k] LASP, Boulder, CO, United States

ARTICLE INFO

ABSTRACT

The SPICAM experiment onboard Mars Express has accumulated during the last decade a wealth of observations that has permitted a detailed characterization of the atmospheric composition and activity from the near-surface up to above the exosphere. The SPICAM climatology is one of the longest assembled to date by an instrument in orbit around Mars, offering the opportunity to study the fate of major volatile species in the Martian atmosphere over a multi-(Mars)year timeframe. With his dual ultraviolet (UV)-near Infrared channels, SPICAM observes spectral ranges encompassing signatures created by a variety atmospheric gases, from major (CO_2) to trace species (H_2O, O_3). Here, we present a synthesis of the observations collected for water vapor, ozone, clouds and dust, carbon dioxide, exospheric hydrogen and airglows. The assembled climatology covers the MY 27–MY 31 period. However, the monitoring of UV-derived species was interrupted at the end of 2014 (MY30) due to failure of the UV channel. A SO_2 detection attempt was undertaken, but proved unsuccessful from regional to global scales (with upper limit greater than already published ones). One particular conclusion that stands out from this overview work concerns the way the Martian atmosphere organizes an efficient mass transfer between the lower and the upper atmospheric reservoirs. This highway to space, as we name it, is best illustrated by water and hydrogen, both species having been monitored by SPICAM in their respective atmospheric reservoir. Coupling between the two appear to occur on seasonal timescales, much shorter than theoretical predictions.

© 2017 The Authors. Published by Elsevier Inc.
This is an open access article under the CC BY-NC-ND license.
(http://creativecommons.org/licenses/by-nc-nd/4.0/)

1. Introduction

The Spectroscopy for Investigation of Characteristics of the Atmosphere of Mars (SPICAM) instrument is a dual ultraviolet in-frared spectrometer that was designed to retrieve the abundances of a set of major and minor species of the Martian atmosphere. Onboard the Mars Express mission, SPICAM has had the capability to perform observations with a variety of geometrical configurations; monitoring the column-integrated abundances of ozone, water vapor and aerosols in a nadir-looking mode, as well as their vertical distribution between ~10 and 150 km using stellar and solar
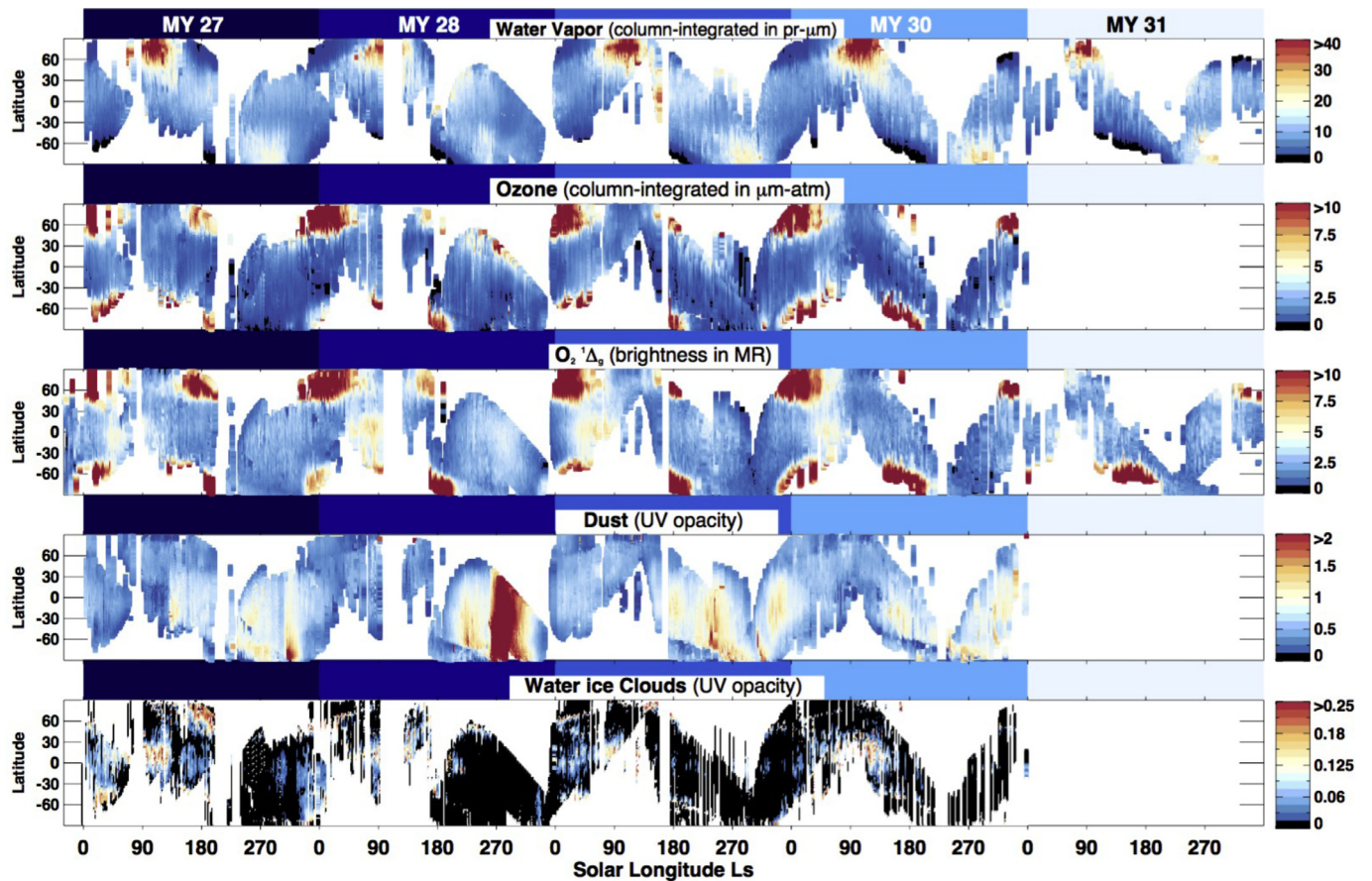
Fig. 1. A compilation of five Martian years of observations by SPICAM in a nadir looking mode. The figure displays zonally averaged values as a function of solar longitude (Ls) of the retrieved (from top to bottom) water vapor, ozone, molecular oxygen singlet delta daytime emission in the near infrared, and dust as well as water ice opacity at 250 nm. The degradation of the UV channel has prevented reliable derivation of ozone and dust/clouds in the ultraviolet during MY31. The unit for each quantity, whose scale is plotted on the right hand-side, is given in brackets.

Note the high degree of repeatability in the seasonal behavior of all quantities, to the exception of dust during southern summer. Note also that displayed abundances have been averaged out of a variety of local times, from morning to afternoon.

occultations. In a dedicated limb staring mode where the Mars Express spacecraft remains in a fixed inertial position, SPICAM is used to infer the density of hydrogen atoms from 200 up to 10 000 km of altitude while relying on the resonantly scattered solar photons at the Lyman-alpha emission line at 121.6 nm of Hydrogen atoms. This same mode of observation is used for the identification of a variety of airglows, some of them being associated with the presence of auroras, as detected for the first time by SPICAM above the magnetic field crustal anomalies (Bertaux et al., 2005a). Since Mars Express orbit insertion on December 23, 2003, SPICAM has operated continuously, accomplishing one of the longest surveys to date of the Martian atmosphere (see Fig. 1), pursuing the reference climatology established by the Mars Global Surveyor (MGS) mission that started near the end of the 20th century and paving the way to the Imaging Ultraviolet Spectrograph (IUVS) onboard the Mars Atmosphere and Volatile and Evolution (MAVEN) that has been operating since September 2014.

The purpose of this paper is to provide an overview of the main scientific results that have been collected thanks to the multi-annual monitoring made by SPICAM. Several results described in this manuscript are presented in greater depth in companion articles that specifically address a particular theme of the SPICAM observations (Trokhimovskiy et al., 2015; Lefèvre et al., in preparation, 2017; Guslyakova et al., 2016). This article is organized around the following topics:

- *Lower atmosphere* sounding including observations and mapping of water vapor, ozone, O_2 and aerosols.

- *Middle atmosphere* sounding with a characterization of the CO_2, O_2, O_3 and aerosols from 50 to 150 km as well as NO emissions subsequent to N and O atoms recombination.
- *Upper atmosphere* sounding to infer the concentration of hydrogen and oxygen atoms above the exobase.

2. Instrument status

2.1. Instrument description

The SPICAM set-up comprises separate ultraviolet and near-infrared channels in one optical unit both connected to the same Data Processing Unit. For the interested reader, detailed technical descriptions of the instrument can be found in Bertaux et al. (2006) and Korablev et al. (2006a).

The ultraviolet channel uses an optical entrance of 4 cm diameter feeding an off-axis parabolic mirror focusing the observed scene at the focal plane. The instantaneous field of view (IFOV) is limited at the focal point of the parabolic mirror by a 50 μm wide retractable slit that extends over an angular aperture of 2.8°, equivalent to about two pixels on the UV detector. In the upper most portion of the slit, a 10 times wider aperture allows for the observations of fainter sources at the expense of degraded spectral resolution. Spectral dispersion is accomplished by a concave holographic toroidal grating imprinting the diffracted orders at the entrance of an MgF_2 window covering a solar blind CsTe photocathode with zero quantum efficiency beyond 320 nm. An additional sapphire filter is glued above the window and covers it
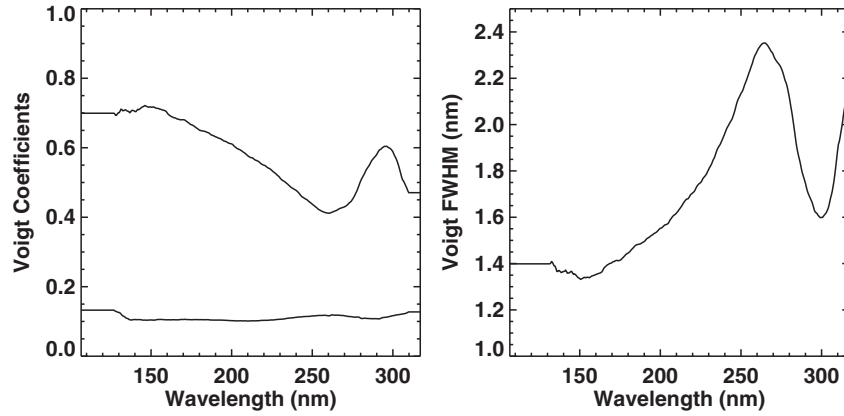
Fig. 2. (Left) Wavelength-dependent parameters of the Voigt profile $H(a,u)$ that best fits the SPICAM UV channel Point Spread Function. The solid line refers to the damping parameter a while the dashed line is for the offset u/x. (right) Estimate of the full width at half maximum of the Voigt profile and its dependence to wavelength. The brutal variation above 250 nm is due to the effect of the sapphire window glued at the entrance of image intensifier, combined with the rapidly changing index of refraction of MgF2 at short wavelength. The absence of the window (pixels > 270) improves the focusing in the remaining range.

partially, preventing overlapping of diffraction orders and Lyman-α stray light. This defines the entrance of the image intensifier that consists of a Micro Channel Plate (MCP) whose gain is adjusted by a high voltage level ranging from 500 to 900 V. The CCD detector is a Thomson TH7863 with 288 × 384 pixels (23 μm pitch) cooled by a thermo-electric device ensuring lower dark current. The spectral resolution of the instrument is wavelength dependent; it exceeds 1.25 nm over the entire range, increasing up to 2.3 nm around 260 nm (see Fig. 2).

The focal length of the UV telescope is such that one CCD pixel covers a IFOV of 0.01° × 0.01° The narrow part of the slit of the spectrometer is 0.02° wide by 1.9° long while the wide part is 0.2° wide by 0.98° long. To reduce the telemetry burden, only five binned areas of the detector are transmitted at the end of each acquisition. These binned areas consist of summed lines of pixels that correspond to contiguous areas in the observed scene. It is thus possible to obtain the spatial variation of the UV spectrum along the axis of the slit. The number of lines per bin is defined at commanding and is usually chosen to accommodate the expected brightness of the observed scene. For a point source such as a star, the standard binning covers 16 lines of pixels while for an extended source such as the Mars surface, the binning is reduced to 4 lines on the detector.

The near-infrared channel of SPICAM has inaugurated the first use of acousto-optic tunable filters (AOTF) in deep space. Built by IKI, the SPICAM near-IR channel accommodates a relatively high-resolution spectrometer in a very light design (< 800 g). The AOTF operating principle relies on producing interferences between the incident optical beam and an acoustic wave in a birefringent medium (TeO$_2$). The input optical beam sustains a volume diffraction that isolates two diffraction orders away from the un-diffracted fraction of the input beam. The acoustic wave propagation inside the TeO$_2$ crystal is generated by a radio-frequency (RF) controller that synthetizes the frequency at which the transducer must be excited to create an acousto-optic interference inside the crystal. Because there is a strict relation between the input RF frequency and the diffracted wavelength, one is able to retain a specific wavelength selected within a range equivalent to an octave of the RF controller. Because the energy remains concentrated within the first (+ 1 and −1) diffracted orders, such devices do not require additional filters to reject higher diffraction orders. This leads to a simple and adaptable spectral analyzer (any wavelength can be accessed instantaneously). There is no slit in the AOTF spectrometer, increasing the throughput compared to traditional grating spectrometers. In turn the

AOTF relies on a progressive scanning of the wavelengths of interest to reconstruct a given spectrum thus reducing the overall efficiency.

With this set-up, the near-IR channel of SPICAM is capable of isolating at each acquisition a 0.5–1.2 nm bandwidth within the accessible 1 to 1.7 μm range. In the range of the water vapor band the resolving power $\lambda/\Delta\lambda$ is ~2000. Wavelengths are registered sequentially with the increment of ~0.3 × $\Delta\lambda$ windowing or loose sampling allows reducing the duration of measurements. To better characterize atmospheric aerosols, the continuous absorption is also measured at several distant wavelengths. The IFOV is circular, and amounts to 1° for nadir measurements, and to ~4 ″ when observing the Sun.

2.2. Calibration and instrument ageing

As explained in Bertaux et al. (2006), we define the sensitivity of the SPICAM UV channel as the sensitivity of the instrument for a stellar source placed at the center of the spectrometer slit. The nominal wavelength assignment is defined accordingly, making it valid for all extended source measurements collected with the slit in place. The so-called efficient area S_{eff} (in cm2) is a wavelength-dependent function of the actual instrument photosensitive area collecting the photons emitted by a point source (see Fig. 3). The displayed S_{eff} curve is obtained when the star signal is integrated over 16 CCD lines (centered on CDD line 144) encompassing roughly 90% of the total signal (the remaining 10% spreading away from the dispersion area). The drop at short wavelength cut-off is due to the opacity of MgF$_2$ window, while the drop at longer wavelength reflects the drop-off of the photocathode.

An updated version of the calibration procedure of the SPICAM UV spectra is given in Snow et al. (2013). We recall here the main expression to be used for converting SPICAM UV detector readouts (in Analog-to-Digital Units, ADU) into physical units (photons × cm^{-2}) for a point source:

$$N_{ADU}/pixel/acquisition = g \times N_p \times \Delta\lambda \times T_i \times S_{eff} \times f_{star}$$

and photons × cm^{-2} × sr^{-1} for extended sources:

$$N_{ADU}/pixel/acquisition = g \times N_p \times \Delta\lambda \times T_i \times S_{eff} \times \omega$$

The number of ADUs N_{ADU} yielded by a pixel during one integration is therefore proportional to the gain of the detector g, the number N_p of photons detected per wavelength unit and per second, the spectral sampling $\Delta\lambda$ (~0.54 nm per pixel) and to the integration time T_i (in second). In case of an extended source, the
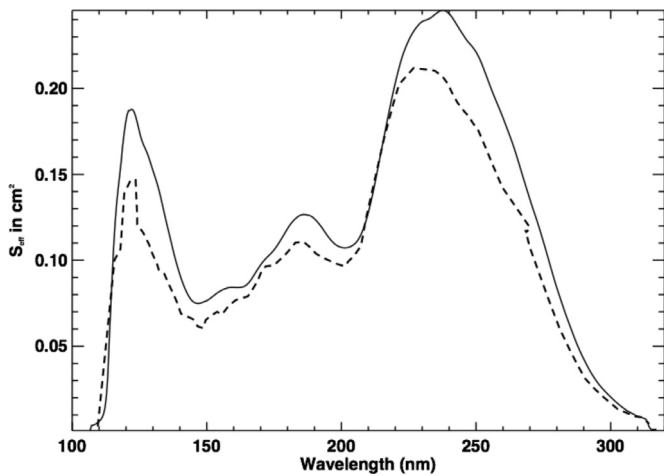
Fig. 3. Updated version of the efficient area *Seff* of the SPICAM UV channel based on the updated calibration procedure established by A. Reberac and reported in Snow et al. (2013). The previously published version of *Seff* (see Bertaux et al., 2006) is shown for comparison in dashed line.

solid angle ω subtended by a pixel (8×10^{-8} sr) needs to be included as an additional multiplicative term. The parameter f_{star} refers to the fraction of the incident photons falling exactly on the pixel. As indicated by Bertaux et al. (2006), a binning of 16 lines of pixel contains around 90% of the stellar light ($f_{star} = 0.9$). The recorded evolution of the instrument sensitivity is shown in Fig. 4 for the 10 years of the SPICAM survey. The plotted quantity is the instrument gain g as a function of the intensifier high voltage. It is clear that the SPICAM UV channel encountered a gradual degradation from late 2011 onwards that eventually led to a > 10-fold reduction of sensitivity, still allowing us to maintain acceptable scientific performances.

2.3. Instrument status

As of December 2014, SPICAM UV channel has ceased returning science data, sending only dark frames instead. This situation is the outcome of a progressive demise of the UV channel whose origin was first identified 9 years before. In January 2006, the SPICAM UV channel started to exhibit an anomalous image intensifier behavior, characterized by multiple sporadic and spurious changes of the high voltage setting during a sequence of observation. The SPICAM UV channel data cleaning process has eventually allowed us to retain all healthy spectra while identifying most ($> 95\%$) of the affected ones. SPICAM Level 0C data in the ultraviolet available on the European Space Agency's Planetary Science Archive have been produced this way, each recorded spectrum being associated with a flag parameter indicating whether the spectrum is infected or not.

For additional details, the reader is invited to consult the Appendix section where a summary is given of the main changes in data processing and in our understanding of the instrument characteristics since the first publication on this topic (Bertaux et al., 2006).

The IR channel, on the other hand, has exhibited a stable behavior throughout the MEX mission, and no noticeable degradation of the IR spectra quality has to be reported at this point.

2.4. Dataset

Since the beginning of its operations at Mars, SPICAM has accomplished more than 12,500 sequences of observations (see Table 1) among which several thousands of atmospheric profiles as well as a continuous multi-annual tracking in nadir mode.

3. Lower atmosphere sounding (0–50 km)

Contrarily to most NASA missions, the ESA Mars Express orbiter does not obey a sun-synchronous orbit and thus nadir mapping covers a variety of local times from morning to afternoon. There is a specific interest for identifying and studying the local time dependence of the species behavior (such as O_3 and H_2O), but the Mars Express orbit does not perform a regular local time sampling and some aliasing with seasonal timescale is difficult to avoid. For this reason, local time dependence is not discussed in the following yet should be the purpose of future in-depth analysis of this dataset.

3.1. Water vapor

• Nadir mapping

The infrared channel of SPICAM has provided a nearly continuous survey of the column-integrated abundance of water vapor since 2004 using the water vapor 1.38 μm absorption band (as described in Fedorova et al., 2006a). This dataset spanning Martian Years 27–31 (see Fig. 1) enables the investigation of both the seasonal and the inter-annual variations of atmospheric water. The radiative transfer model used for the retrieval accounts for multiple scattering caused by dust and clouds. Compared to the original version of the retrieval reported in Fedorova et al. (2006a), the data treatment (Trokhimovskiy et al., 2015) used for the results presented here incorporates a number of improvements mainly related to a better characterization of the instrument calibration and of the model input parameters. The sensitivity of results to aerosol properties, surface albedo, solar spectrum, and water vapor vertical distribution has been carefully evaluated. For instance, neglecting the aerosol scattering biases the inferred water amount by as much as 60–70% during dusty events. Water vapor retrieval is also sensitive to cloud activity especially around aphelion in the tropics. However, the effect of clouds and dust have been included in the retrieval. Information on dust and ice abundances were extrapolated from the published THEMIS dataset (which spans until the middle of MY30-Smith et al., 2009) down to the near-IR range of SPICAM.

SPICAM observations reveal a water vapor seasonal behavior that is to a large extent in agreement with previous monitoring (in particular TES dataset, as revised from Smith, 2004); water column integrated abundance peaks near 60–70 pr. μm in the northern summer polar region as the polar layered deposits get exposed to intensified spring/summer insolation whereas only 20 pr.-μm is observed during the southern summer at the south pole. The equivalent volume of ice sublimating as vapor in the atmosphere is about 0.5 km^3 at the beginning of the year and later builds up to 2.3 km^3 at Ls = 100° at a time when water vapor abundance is found maximum on a global average.

To the exception of the MY28 dust event that is discussed below, SPICAM reveals a water cycle that is stable on average throughout the terrestrial decade monitored. With the revisit of the Mars Atmospheric Water Detector dataset (Fedorova et al., 2010), the picture of a Mars' water cycle evolving in a quasi-stabilized state appears more and more confirmed (Richardson and Wilson, 2002; Montmessin et al., 2004, 2017). Mars's water cycle responds essentially to the large seasonal and spatial variations of insolation over the globe. It is possible that variability may occur on timescales greater than a decade, but the compilation of water vapor measurements made to date suggests the water cycle did not change significantly over more than 20 Mars years.

When comparing Martian Years (Fig. 1), one is able to capture the prominent drop of water abundance that occurs during the dust storm of MY 28. This sudden decrease of water, which was also reported in CRISM data (Smith et al., 2009), cannot be
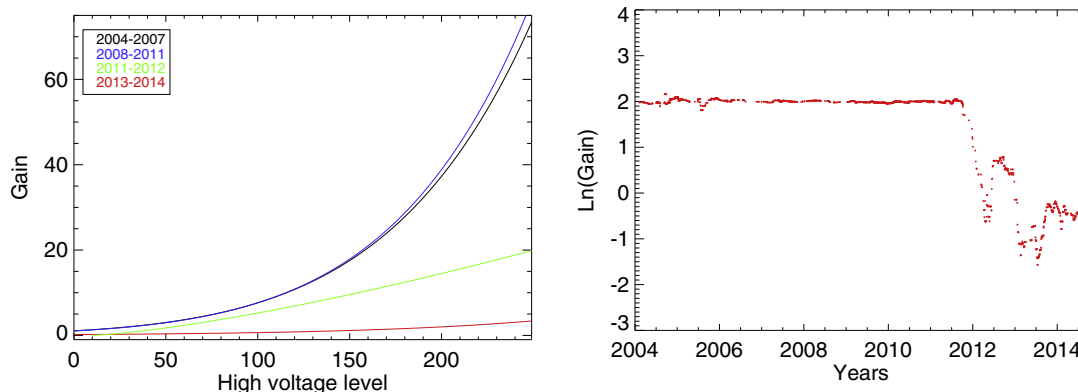
Fig. 4. (Left) SPICAM UV channel intensifier gain curve as a function of the high voltage level (1–28 = 256). (right) Gain (in logarithmic scale) evolution with time for a fixed value of high voltage. The curves on the left distinguish between various periods during the mission, highlighting the relatively stable behavior from 2004 to 2011, and the significant loss of sensitivity that occurred in 2011, after which time, SPICAM intensifier lost a rough factor of 10 in efficiency. Near the end of 2014, SPICAM UV channel ceased to transmit observed signal, suggesting the loss of the intensifier.

Table 1
Breakdown of SPICAM observations against modes of operation as performed since the beginning of Mars Express operations until the end of 2014 when the UV channel stopped nominal operations.

Channel	Nadir	Limb	Stellar occultation	Solar occultation	Phobos/deimos	Calibration	Sky	Earth	Comet	Total
UV	3553	1724	4625	1096	238/67	866	261	5	19	12,454
IR	3549	1494	1855	1036	236/67	12	27	0	16	8292

attributed to measurement biases caused by shielding of the water molecules by dust. It appears to reflect an actual drop of atmospheric water near or above the surface during the dust storm. Dedicated radiative transfer calculations indicate that water vapor retrieval based on the optically thin 1.38 μm absorption band is mostly sensitive to the water present in the first kilometers of the atmosphere above the surface. We speculate that the observed decline of the water abundance during MY28 is consistent with enhanced adsorption by the Martian regolith. The higher adsorbing capacity of the regolith under conditions of globally spread dust storms has been predicted by Böttger et al. (2004, 2005) based on Global Circulation Model (GCM) computations and appears to be corroborated by the present measurements. Note that clues for a diurnal "breathing" of the regolith at a local scale could not be supported by the available SPICAM measurements due to the inadequate Mars Express local time coverage.

It is to be noted that within the context of Mars Express, an important endeavor of instrument cross-comparison was undertaken in order to understand the differences of retrieved water vapor column abundances. The Observatoire pour la Minéralogie, l' Eau, les Glaces et l' Activité (OMEGA) (Bibring et al., 2005; Encrenaz et al., 2005) and the Planetary Fourier Spectrometer (PFS) instruments (Formisano et al., 2006; Fouchet et al., 2007) also provide measurements of water vapor and these were compared to SPICAM (Tschimmel et al., 2008). This comparison study allowed for a quasi-convergence of all Mars Express instruments yet some departures (within 20–30%) remained that the very nature of observations (e.g. spectral range) could partly explain. At that time, SPICAM was clearly standing out from these other measurements, but an in-depth reanalysis led to realigning SPICAM with the rest of Mars Express (Trokhimovskiy et al., 2015).

• Vertical profiles from solar occultations

SPICAM delivered the first monitoring of the water vapor vertical profile between ∼10 and 100 km during a whole Martian year (Fedorova et al., 2009; Maltagliati et al., 2011, 2013). The three occultation campaigns presented here, allow us to examine a somewhat unexpected behavior of water vapor vertical distribution (Fig. 5). Water vapor is found less abundant and more confined in the lower atmosphere during northern spring/summer, an expected result when considering that water vapor should remain sequestered below the condensation level (hygropause). However, as demonstrated by previous SPICAM studies, the vertical distribution is not entirely dictated by the vapor saturation conditions: large excesses of saturation have been observed, especially at mid-latitudes in the northern hemisphere spring (Maltagliati et al., 2011). In contrast, the warmer southern spring appears associated with a higher vertical mobility for water vapor (as illustrated by Fig. 6), a characteristic that was observed especially after Ls = 240° There, recurrent features of discrete layers of water vapor with > 100 ppmv mixing ratio have been reported above 60 km.

While the water vapor profiles appear to reflect the large temporal and spatial variabilities of the Martian climate, they also show sensitivity to more localized and short-term meteorological events. Abrupt variations (within a day or so) of water vapor abundance and in vertical distribution can be identified. Water upsurges, appearing suddenly within few Martian days, were observed three times in MY29 as described in Maltagliati et al. (2013) and reproduced here in Fig. 6. Similar short-term variations affect the aerosol profiles, acquired by SPICAM simultaneously with water, suggesting that transport phenomena affect water and aerosols likewise. Aerosol upsurges are observed systematically in conjunction of those occurring with water vapor and detached layers of aerosols are often coupled with the water ones. These observations demonstrate the importance of the vertical distribution as crucial diagnostics for key processes in the Martian water cycle and climate as a whole.

3.2. Ozone

• Nadir mapping

Between 2004 and 2011, SPICAM observations in nadir viewing provided a continuous and near-complete coverage of the ozone column distribution, one of the largest database of Martian ozone to date. The ozone column is retrieved from the UV channel simultaneously with the mean (210–290 nm) dust opacity and surface albedo. Perrier et al. (2006) presented an initial version of the retrieval algorithm to process the first 1.2 Martian year of SPICAM
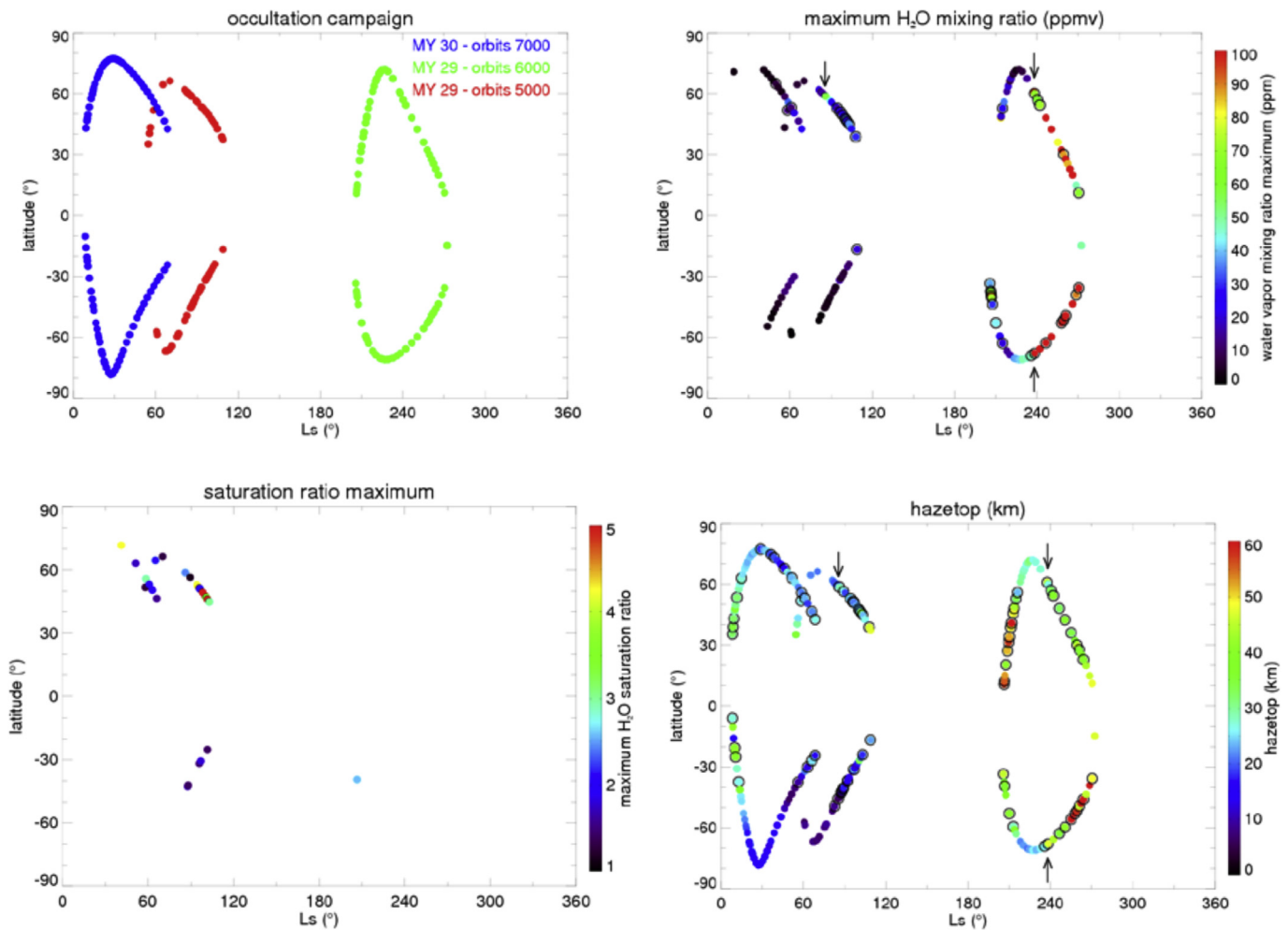
Fig. 5. (Top left) Geographic and seasonal distribution of the three Mars years of infrared solar occultations compiled in this work. (Top right) maximum value of the water vapor volume mixing ratio detected for each orbit. Only the orbits with positive detection of water vapor are plotted. The orbits with a black circle exhibit a detached layer. The arrows indicate the moments of the sudden upsurges of water (see text). (Bottom left) maximum value of the water saturation ratio for the orbits where supersaturation is detected. (Bottom right) hazetop, defined as the altitude where the aerosols' optical depth drops to 1 from below. The black circles identify orbits with detached layers, and the arrows mark the position of the upsurges.
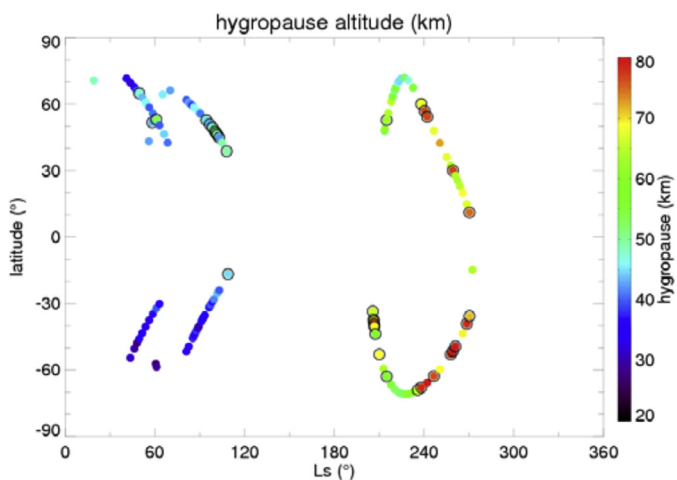

Fig. 6. Compilation of all the derived values of the hygropause altitude, defined as the level above which water vapor can no longer be detected.

operation. Their method used a full radiative transfer model of the Mars atmosphere and accounted for multiple scattering caused by dust and clouds. Recently, the UV nadir dataset has been entirely reprocessed with an improved version of the algorithm. Thanks to a better characterization of the efficient area S_{eff} and the improved modeling of stray light in nadir spectra, the ozone retrieval now relies on the absolute UV reflectance observed by the instrument. Hence, it no longer requires the use of a so-called "reference spectrum" above Olympus Mons as in Perrier et al. (2006). This eliminates the risk of systematic error due to the unwanted presence of dust or clouds in the reference spectrum, and allows using areas of the CCD that are not necessarily the same as those used to record that spectrum. Other improvements in the method include revised optical properties for aerosols and Rayleigh scattering, as well as a shorter time averaging of nadir spectra (30 s vs. 50 s) in order to increase the spatial resolution of the measurements.

Fig. 1 shows the zonally averaged ozone column distribution obtained from SPICAM for three consecutive Martian years of observation. Compared to Earth, the strong seasonal and spatial variability of ozone (a factor of ~100 as opposed to ~3 on our planet) is a striking feature of Mars photochemistry. As for the pioneering measurements of the Mariner missions (e.g., Barth et al., 1973), the maximum ozone columns measured by SPICAM are near 40 μm-atm and are found at high latitudes in winter/spring. By contrast, polar ozone shows columns usually less than 1 μm-atm in summer. At mid-to-low latitudes, the ozone annual cycle is of much more limited amplitude. SPICAM indicates values in general of the

order of 1 μm-atm or less, except around Mars aphelion when a weak maximum ($\sim$3 μm-atm) is identified. This ozone cycle is in good agreement with HST and Earth-based measurements (Clancy et al., 1999; Fast et al., 2006), as well as with the observations by the MARCI imager on board MRO (Clancy et al., 2016).

An indirect measurement of the ozone column may also be accomplished via the $O_2(a^1\triangle_g)$ dayglow detected with the IR channel. This airglow is produced during ozone photolysis by solar UV radiation. The $O_2(a^1\triangle_g)$ molecule, that is an excited state of O_2, can subsequently emit a photon at 1.27 μm or be quenched by CO_2. The latter process dominates at altitudes below 20 km and therefore dayglow only reflects the ozone abundance above 20 km. The first seasonal evolution of the $O_2(a^1\triangle_g)$ emission has been obtained from the SPICAM data and presented by Fedorova et al. (2006b). This work was later extended and resulted in a continuous climatology of the $O_2(a^1\triangle_g)$ dayglow for six Martian years from the end of MY26 to MY32 (Guslyakova et al., 2016). The $O_2(a^1\triangle_g)$ intensity is traditionally expressed in MR (MegaRayleigh) unit, where $1R = 10^6$ photon cm^{-2} s^{-1}(4π ster)$^{-1}$. Fig. 1 shows the zonally-averaged emission rate for five Martian years. The good correlation with the ozone seasonal behavior is obvious. Maximal values of the $O_2(a^1\triangle_g)$ dayglow reaching 30 MR are observed in early northern and southern springs in both hemispheres. Near the equator a spring maximum of 7 MR is observed for all years. The emission intensity is minimsal in the southern hemisphere in summer with values of 1–2 MR. Together with the ozone column density determined with the UV channel, the $O_2(a^1\triangle_g)$ emission measured with IR channel can provide constraints on the vertical distribution of ozone from nadir measurements.

The distribution of ozone in Fig. 1 shows an obvious anticorrelation with that of water vapor. This inverse relationship is well understood from a theoretical point of view. The strongest sink of odd oxygen (O and O_3) is accomplished by the reactions with the hydrogen radicals (H, OH, and HO_2) produced by the photolysis and oxidation of water vapor. The efficiency of these processes is such that the chemical lifetime of ozone during the day is, at low-to-mid latitudes, usually shorter than 1 h in the low atmosphere. This tight coupling between O_3 and H_2O explains the near-zero ozone columns observed by SPICAM when water vapor sublimes from the polar caps in summer. It also explains the tropical O_3 maximum observed around aphelion, when the confinement of H_2O near the surface allows more O_3 to form above the hygropause. In the wintertime high latitudes, the lack of water vapor and limited sunlight prevent almost completely the production of HO_x. In these conditions, the chemical lifetime of ozone may increase up to several days. Ozone can accumulate inside the dry polar vortices, and atmospheric transport plays a major role. Three-dimensional model simulations have shown (Lefèvre et al., 2004) that wave activity explains well the considerable day-to-day variability in polar ozone measured by SPICAM (Perrier et al., 2006) and MARCI (Clancy et al., 2015).

Ozone is therefore a sensitive tracer of both transport processes (at polar latitudes) and of the HO_x chemistry that stabilizes the CO_2 atmosphere of Mars (everywhere else). With their quasi-pole-to-pole coverage, SPICAM measurements have already indicated that heterogeneous chemical processes involving HO_x may be important to explain quantitatively the ozone amounts retrieved from the instrument (Lefèvre et al., 2008). Further constraints on photochemical models are anticipated from the unique capability of SPICAM to retrieve simultaneously the ozone and water vapor columns, which will be presented in a detailed study currently in preparation.

• Ozone profiles derived from stellar and solar occultation

A compilation of nighttime ozone profiles was made with SPICAM UV covering the northern spring equinox (solar longitude $L_s = 8°$) to northern winter solstice ($L_s = 270°$) time frame

(Lebonnois et al., 2006). These observations along with theoretical studies have allowed characterization of the nighttime ozone vertical distribution at mid-to-low latitudes, yielding a clear distinction between a near-surface layer, typically perceptible below 30 km, and an elevated layer only present around aphelion. As explained in a number of previous studies (Lefèvre et al., 2004; Lebonnois et al., 2006), the near-surface layer existence is promoted by ultraviolet screening by CO_2 molecules, which inhibits HO_x production through H_2O photolysis. The elevated layer (> 20 km of latitude) of ozone appears essentially at night as O_3 is rapidly photolized after sunrise. Its magnitude is controlled by HO_x concentration above 25 km. For this reason, seasonal variations of the water saturation level exert a strong modulation of the elevated layer of ozone in the tropics, forcing O_3 to maximize around the northern summer solstice when temperatures are lowest and to vanish soon after $L_s \sim 130$. In a recent study (Montmessin and Lefèvre, 2013), the analysis of the ozone profiles observed with SPICAM was extended to the polar regions and evidence was reported for the existence of an ozone layer that has been observed repeatedly during three consecutive Martian years in the southern polar night at 40–60 km in altitude, with no counterpart observed at the north pole. Comparisons with global climate simulations indicate that this layer forms as a result of the large-scale transport of oxygen-rich air from sunlit latitudes to the poles, where the oxygen atoms recombine to form ozone during the polar night. However, transport-driven ozone formation is counteracted by the destruction of ozone through reactions with hydrogen radicals, whose concentrations vary seasonally on Mars, reflecting the seasonal variations of water vapor vertical distribution in the tropics, as discussed above. The observed dichotomy between the ozone layers of the two poles, with a significantly richer layer in the southern hemisphere, is a robust indicator of the coupling between chemistry, transport and water cycle processes.

Ozone profiles can also be derived from SPICAM UV solar occultations, which were analyzed for the first time by Määttänen et al. (2013). However, these authors only discussed the derived aerosol and cloud vertical distribution. Here, we present a first subset of the ozone profiles obtained from solar occultation that we plan to analyze in the future against the water vapor profiles retrieved simultaneously with the near IR channel. In Fig. 7, we compare results for ozone as obtained from stellar (lower panel) and solar occultations (upper panel) for the latitude band 0–30°S. The plot in the lower panel is an extended version of the figure presented by Lebonnois et al. (2006). Whereas the stellar occultation pertains to a wide range of local times in the night, solar occultation only deals with the morning and evening terminator conditions where the chemical regime is in a transient state. The upper panel of Fig. 7 shows that a similar layer at the same altitude range is observed both at night and near terminator. However, the layer at the terminator appears significantly weaker than the night-time layer. Lebonnois et al. (2006) discussed the daily cycle of ozone and noticed that the ozone layer around 30–45 km altitude forms rapidly after sunset, building up until sunrise. Since solar occultations occur at sunset/sunrise, the layer has either not fully formed (sunset) or has already started to withstand photolysis (sunrise), explaining the lower amounts obtained in the case of the solar occultation.

A joint analysis of the SPICAM ozone and water vapor products in solar occultation, the latter being provided by the SPICAM IR channel (Maltagliati et al., 2011, 2013), will enable a comprehensive assessment of the theory governing the ozone chemistry on Mars.

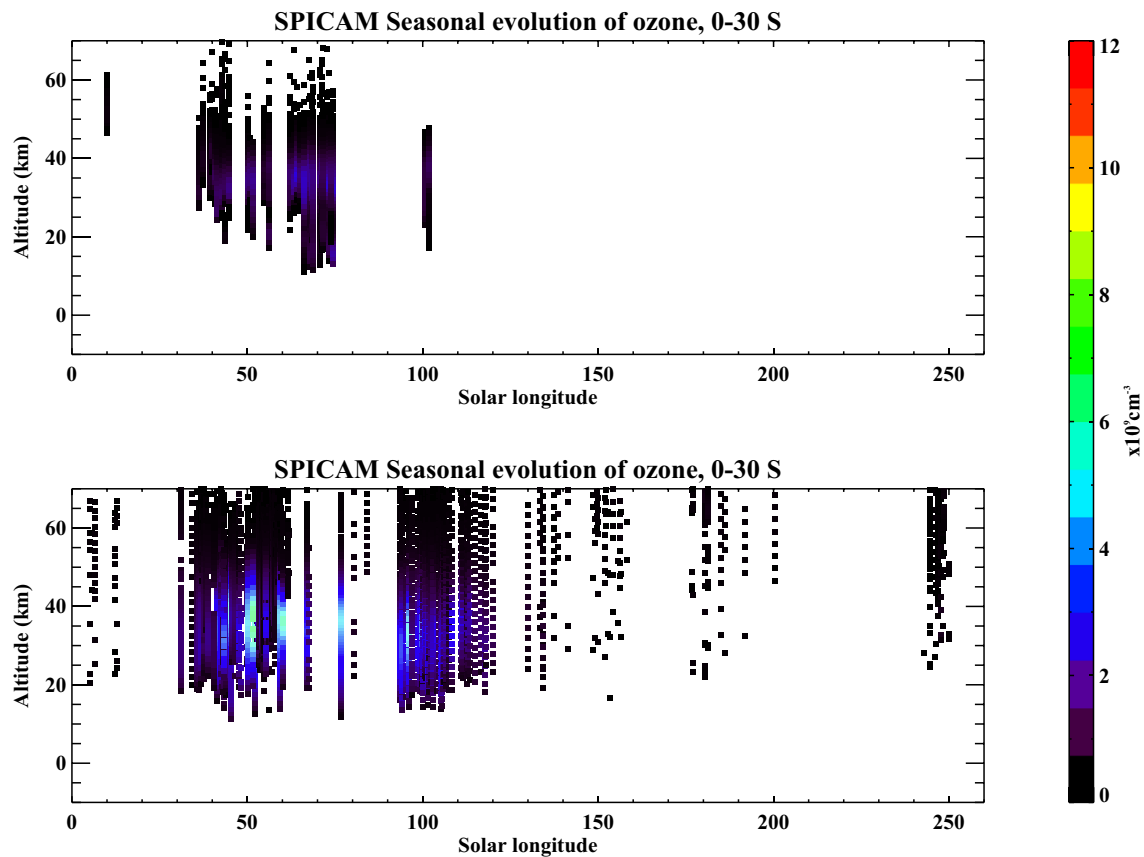### 3.3. Dust and clouds

• Nadir mapping

Fig. 7. Seasonal evolution of ozone concentration profiles in the latitude band 0–30°S. (Upper panel) Solar occultations in the UV. (Lower panel) Stellar occultations in the UV. The color code shows ozone concentrations in 10^9 molecules $\times$ cm^{-3}. (For interpretation of the references to color in this figure legend, the reader is referred to the web version of this article).

The SPICAM UV spectral domain allows the detection of airborne dust and cloud particles. Ice clouds and dust both play a role in the radiative transfer but their effects are very different in the UV. Ice clouds are bright features that lie aloft against a dark and absorbing surface. Dust on the other hand possesses optical properties that are comparable to those of the surface, making it more complicated to distinguish. Nadir UV data from SPICAM UV observations in nadir mode was also used to study Martian aerosols.

Dust abundances vary greatly depending on the season and location on the planet (see e.g. Smith, 2004). During most part of the year, dust is present in relatively low-to-moderate quantity and is located low in the atmosphere (below 30 km). However the planet undergoes regular dust storms, especially during southern spring and summer, when larger amounts of dust are lifted up in the atmosphere and can reach altitudes up to 60 km. The dust storms season happens typically during the $L_s = 180$–330° timeframe. Nadir UV SPICAM data has provided an opportunity to improve the knowledge about the Martian dust optical properties in the UV domain (see the first study in Perrier et al., 2006). Analysis of the SPICAM nadir spectra acquired during a few dust storms allowed us to estimate optical properties, such as single scattering albedo ω and asymmetry factor g (Mateshvili et al., 2007). The reported values are $\omega = 0.6 \pm 0.045$, $g = 0.88 \pm 0.04$ at $\lambda = 213$ nm and $\omega = 0.64 \pm 0.04$, $g = 0.86 \pm 0.03$ at $\lambda = 300$ nm. Water cloud optical depth distributions during different seasons were also retrieved (Mateshvili et al., 2006, 2008) and improved in a recent investigation (Willame et al., 2017), which analyzed the complete SPICAM dataset available from MY 26 to the end of MY30. Coupling together the retrievals on these four years offers a relatively

complete overview the Martian annual cloud distribution outside the polar caps (see Fig. 8).

Overall, the ice cloud abundance deduced from SPICAM UV data shows the same features as the ones already reported in the past by a number of authors (e.g. Clancy et al., 1996; Wolff et al., 1999; Smith et al., 2004). In particular, it shows very prominent seasonal variations and spatial distribution (Fig. 8). Martian ice cloud distribution during the yearly cycle is clearly connected with the Martian atmospheric general circulation and the water cycle. During the northern winter, thick clouds cover the Martian North Pole, forming the north polar hood. As spring progresses, clouds retreat together with seasonal ice to the North and only a few stay above the North Pole during summer. The released water vapor rushes towards the equator where it is picked up by the ascending branch of the Hadley circulation. The rising water vapor reaches altitudes where low temperatures and pressures create favorable conditions for cloud condensation. Clouds form the so-called Aphelion cloud belt, which is persistent during the whole northern summer. At the same time, cloud cover grows above the South Pole forming the south polar hood. When the northern fall starts, the north polar hood grows and the south polar hood retreats. Due to the highly elliptical orbit of Mars the southern summer is much warmer than the northern one. During the season of dust storms, clouds disappear almost everywhere surviving only above the North Pole. Only during southern fall rare clouds start to form above high Martian volcanoes and the cloud cycle starts again.

• Vertical profiles from solar occultations

SPICAM IR has provided long-term observations of the Martian aerosols by solar occultation techniques in the near-IR range. During the five Martian years about 880 successful solar occultations
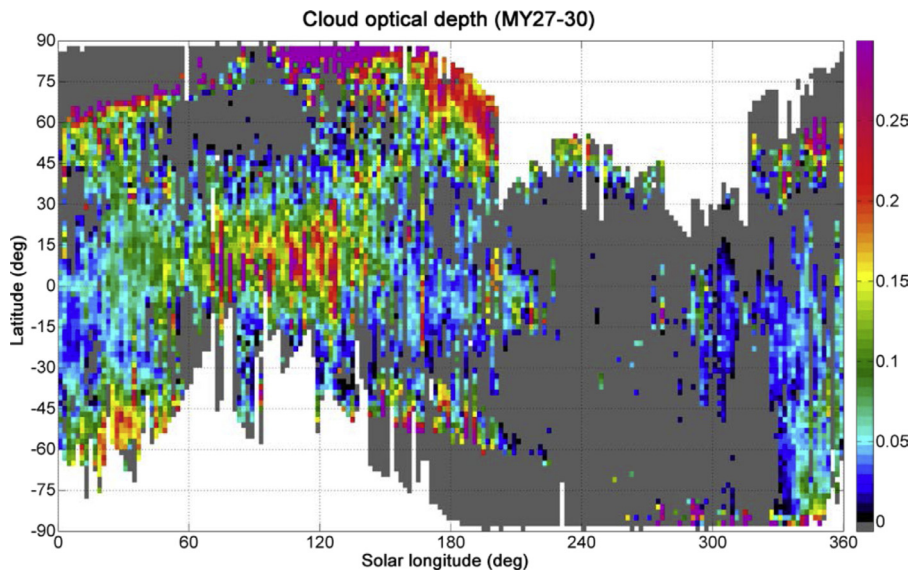
Fig. 8. Zonally averaged cloud optical depth derived from SPICAM nadir UV observations and displayed as a function of latitude and solar longitude. The map assembles four consecutive years of retrieval. Note that the regions covered by ice were rejected from the retrieval.

have been performed. SPICAM spectral range allows simultaneous observations of 1.43 μm CO_2 band for the atmospheric density, the 1.38 μm absorption band of water vapor (as presented above), and the distribution of aerosols with altitude measuring the opacity of the atmosphere in the spectral range from 1 to 1.7 μm. In this configuration, aerosol extinction profiles at 10 different wavelengths have been obtained at altitudes from 0 to 90 km with a vertical resolution of 2 to 10 km depending on the distance to the limb. We consider their seasonal and latitudinal variations (Fig. 9). The interpretation using Mie scattering theory with adopted refraction indices of dust and H_2O ice allows the retrieval of particle size distribution for r_{eff} varying from 0.1 to 1.5 μm as well as number density profiles.

A special attention was paid to the summer in the northern hemisphere, when the water vapor supersaturation in the middle atmosphere has been discovered (Maltagliati et al., 2011). Simultaneous analysis of aerosol extinctions in the UV and IR range at different altitudes during this period has enabled the first direct detection of a bimodal distribution of Martian dust particles with characteristic effective radii of 0.04–0.07 μm and 0.7–0.8 μm (Fedorova et al., 2014). The finer mode with a effective radius between 0.04 and 0.07 μm and a number densities from 1 cm^{-3} at 60 km to 1000 cm^{-3} at 20 km has been detected in both hemispheres. In the southern hemisphere the finer mode extends up to 70 km, whereas in the northern hemisphere it is confined below 30–40 km. The lack of condensation nuclei is consistent with, but cannot fully explain the high water supersaturation levels observed between 30 and 50 km in the same northern hemisphere dataset (Maltagliati et al., 2011). The average size of the fine mode (~50 nm) and the large number density (up to 1000 cm^{-3}) most likely corresponds to Aitken particles ($r < 0.1$ μm). This mode is unstable against coagulation and requires a continuous source of particles to be maintained, in at least one order of magnitude greater than estimations for the meteoric flux. The sedimentation time varies from 100 to 1000 days (for particles 0.1 and 0.01 μm, respectively) at 20 km and 10–100 days at 40 km, and these particles may be transported by the Hadley cell from the northern to the southern hemisphere in the observed period of the summer solstice in the northern hemisphere.

SPICAM solar and stellar occultations in the UV have been recently combined into a four Martian Years dataset on the aerosol vertical distribution. The first analysis of stellar occultations by Montmessin et al. (2006a) has been complemented by an analysis of the solar occultation dataset carried out by Määttänen et al. (2013) comprising more than four Martian years of data. Fig. 10 shows the inter-annual variations of the haze top during Martian Years 27–30 and the detected detached aerosol layers in the atmosphere as a function of season. There is a clear trend for higher haze tops near the equator and during the second half of the year, driven by more vigorous atmospheric circulation at these locations and seasons. The dusty season of southern summer is most evident in the occultations performed in MY28 and MY29. MY27 was relatively average in terms of dustiness and SPICAM indicates a more quiescent second half of the year. In MY30, despite the poor coverage in the tropics, SPICAM was able to capture the low haze tops at higher latitudes. Overall, the low spring haze tops in mid- and high latitudes are faithfully reproduced by the Martian dust cycle, observed in Mars Years 27 (south only), 29, and 30.

Detached layers apparent in most profiles follow the behavior of the haze top, with the lowest layers observed in mid- and high latitudes in the beginning of the year. Around the autumn equinox the layer altitudes increase and remain high throughout the latter half of the year. During the dust storm year MY28 detached layers were observed at very high altitudes (red-orange colors around L_s 260°–300°, Fig. 10). The composition of these layers cannot be directly derived, but some hints could be derived from their UV spectral characteristics by approaching the wavelength behavior by a power law (Määttänen et al., 2013)

3.4. From the search of SO_2 to a preliminary characterization of UV surface albedo

Following the measurements of SO_2 above the clouds of Venus by the companion instrument SPICAV onboard *Venus Express* (Marcq et al., 2011, 2013), a similar approach was applied to SPICAM data in order to identify SO_2 in the Martian atmosphere and potentially explore ongoing outgassing, aiming in any case at better constraining SO_2 presence or its absence thereof. Previous work on the subject from Earth-based instruments (Nakagawa et al., 2009; Krasnopolsky, 2005) only derived upper limits on the order of 1 ppbv on a disk-averaged scale. Preliminary modeling showed that SPICAM sensitivity to SO_2 was on the order of 10 to 100 ppbv in clear dust opacity conditions ($\tau < 0.5$), but SPICAM
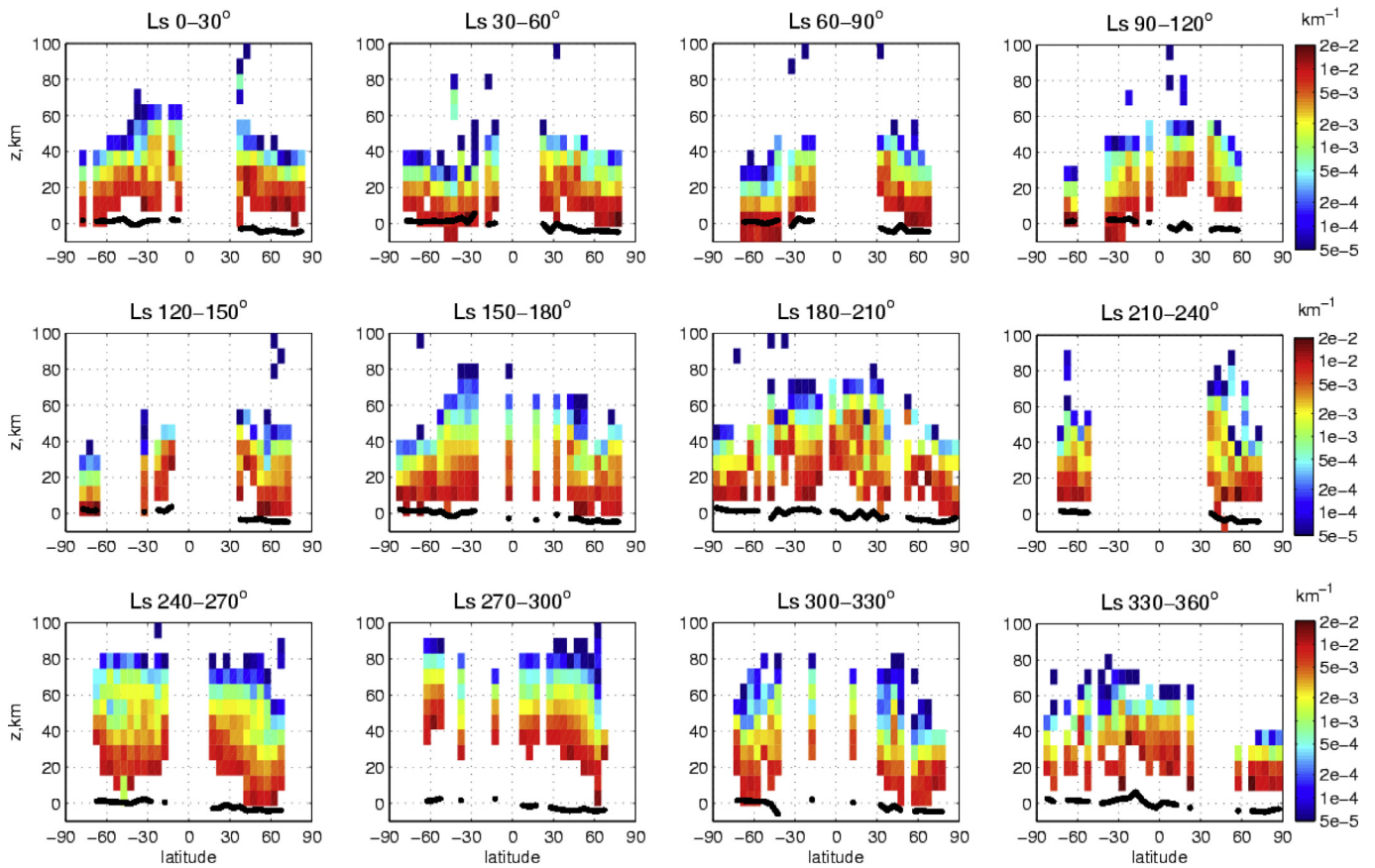
Fig. 9. Seasonal and spatial distribution of the extinction (km-1) vertical profiles at 1094 nm averaged on a grid 30° of Ls × 5° of latitude × 6 km of altitude for 4 MY (MY27-31) from orbit 1200 to orbit 12,166.
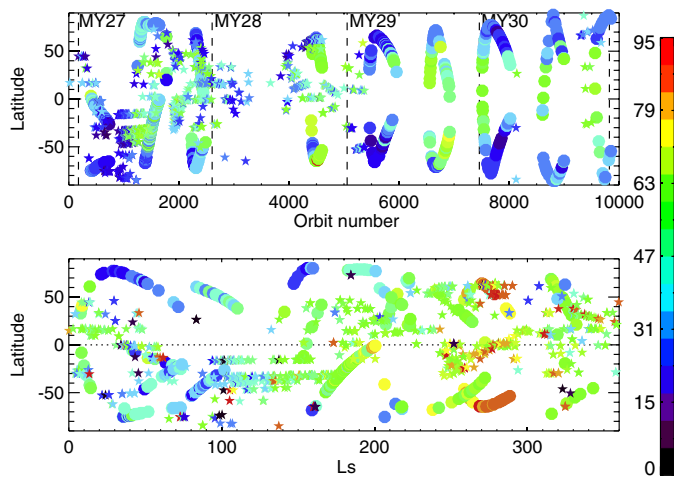

Fig. 10. (Top panel) Interannual variations of the hazetop defined as the altitude at which the aerosol line-of-sight integrated opacity drops to a value of 1 for the first time starting from the bottom of the profile, and (bottom panel) detached layer altitudes analyzed from stellar (stars) and solar (circles) occultations in the UV. (For interpretation of the references to color in this figure legend, the reader is referred to the web version of this article).

Fig. 11. The surface radiance factor of Mars (colored lines) in the UV as derived from 3 UV channel observations and a comparison with the radiance factor deduced for Phobos. (For interpretation of the references to color in this figure legend, the reader is referred to the web version of this article).

was nonetheless used to spot local enhancements since SO_2 is expected to be locally and temporally variable due to its putative sources (sporadic volcanism) and sinks (fast photolysis). However, SO_2 may have been detected at such levels in its strongest band near 210 nm where the Sun's brightness sharply decreases with decreasin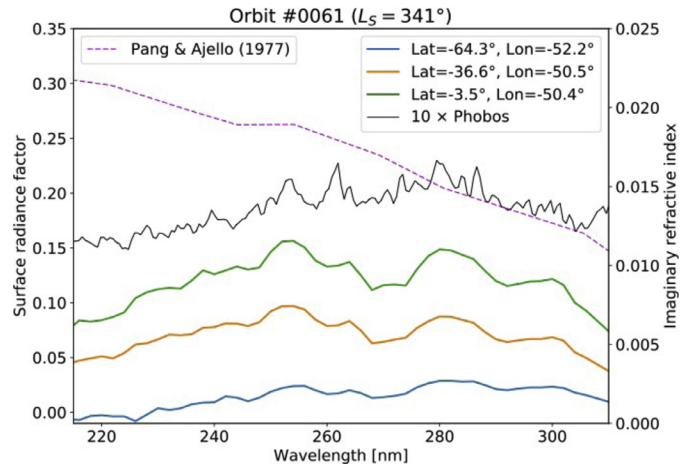g wavelength. The imperfect removal of stray light makes these detections dubious. It is more likely that SPICAM has essentially confirmed the previously derived upper limits – with the most recent estimates established by Encrenaz et al. (2011) who obtained 0.3 ppbv globally and 2 ppbv locally.

An interesting by-product of this detection attempt was to derive spectral UV albedos of the Martian surface (Fig. 11): the radiative transfer model adapted from Perrier et al. (2006) can be used to simulate reflectance spectra taking into account dust and
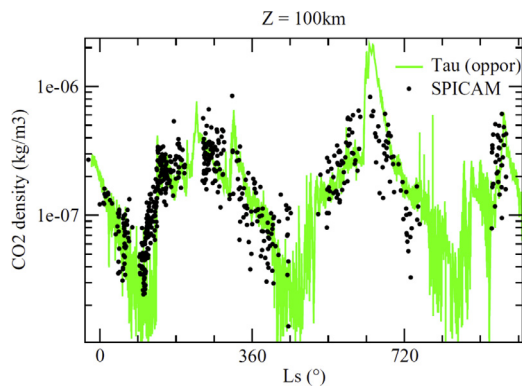
Fig. 12. (Black dots) CO_2 density measured by stellar occultation at 100 km above the Mars zero datum (areoid) between January 2004 (MY26, Ls=333° here shown at Ls =−27°) and February 2011 (MY29, Ls=238° here shown at Ls=958°). Only the data obtained below 50° latitude are shown. (Green curve) A synthetic density $\rho = (5\tau - 2)$ x 10^{-7} directly derived from the visible aerosol opacity τ measured by the Opportunity rover camera (Lemmon et al., 2004). (For interpretation of the references to color in this figure legend, the reader is referred to the web version of this article).

Fig. 13. CO_2 density measured by stellar occultation at 100 km during MY27 (black dots) compared with predictions from an improved LMD Global Climate Model (Madeleine et al., 2011, 2012; Navarro et al., 2014) using a dust climatology compiled for MY27 (Montabone et al., 2017, submitted for publication). The agreement is much better than with the previous version of the GCM (see Fig. 11 in Forget et al., 2009).

O_3 UV opacities but with ground albedo set to spectrally constant values bracketing the observed reflectance spectrum (typically 0 and 0.2). In the single scattering approximation (valid where dust opacity is low enough), it can be shown that there is a linear relationship between the observed radiance and the surface albedo. The two simulated, bracketing radiance factors can then be used to derive a spectrum of the UV surface albedo. Several such derived albedos are shown in Fig. 12. They are consistent with UV dust albedo derived by Pang and Ajello (1977) beyond 280 nm, but differ at shorter wavelengths and exhibit a narrow signature in the 270–290 nm interval. For the sake of comparison, the reflectance of Phobos as deduced from the numerous dedicated observations of the Martian satellite is also displayed in Fig. 11. It is rather remarkable to find that Phobos albedo depicts a spectral behavior akin to the one found for Mars surface.

4. Middle atmosphere sounding (50–150 km)

4.1. Temperature and density profiling using stellar occultation in the UV

The high sensitivity provided by the observations of the setting or rising of UV bright stars through the atmosphere with SPICAM has provided the first remote sensing measurements of the density and temperature in the Martian middle atmosphere, between 70 and 130 km (Quemerais et al. 2006; Forget et al., 2009). The only other observations in that altitude range are the *in situ* density measurements performed by entry probes and aerobraking spacecrafts. CO_2 absorbs stellar radiation between 120 and 190 nm and allows a high sensitivity for a wide range of pressures, between 10^{-6} and 1 Pa. However, at pressure higher than 0.1 Pa (i.e. below 60 and 70 km), it has been found that the retrieved densities can be significantly underestimated as the stellar spectrum gets fully absorbed in its Far Ultraviolet part (short ward of 180 nm), and the temperatures overestimated. No reason has been found so far to explain this "warm bias" although several potential causes have been explored (CO_2 cross section dependence on temperature, atmospheric refraction).

The first 616 usable profiles obtained for a wide range of latitude and longitude over a little more than one Martian year (MY 27) have been analyzed by Forget et al. (2009). Since MY27, many more occultation observations have been performed, although in
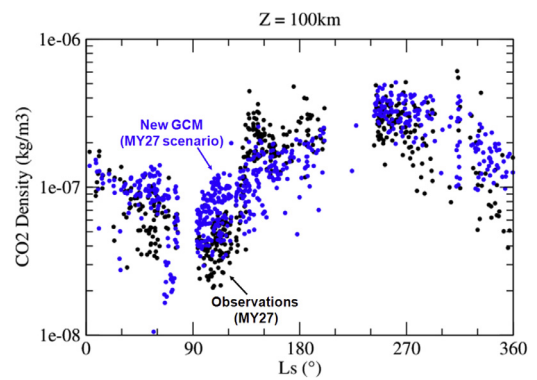
many cases the measurements have been affected by the spurious intensifier spikes described previously (see Appendix).

Fig. 12 shows a compilation of the density measurements interpolated at 100 km above the Mars geoid (areoid) between the end of Martian Year 26 until mid-Martian Year 29. As analyzed in Forget et al. (2009), atmospheric densities exhibit large seasonal fluctuations mostly due to variations in the dust content of the lower atmosphere which controls the temperature, and thus the atmospheric scale height, below 50 km. The direct correlation between the air density in the upper atmosphere and the lower atmosphere dust loading is illustrated by the green curve in Fig. 12 which is a linear function of the visible dust opacity as measured by the camera on the Opportunity rover (Lemmon et al., 2004). The response of the upper atmosphere of Mars to lower atmospheric dust storms has also been studied using SPICAM data and other datasets by Withers and Pratt (2013).

In Forget et al. (2009), comparison of the observed variations to the LMD Global Climate Model (GCM) revealed significant disagreement mostly due to an inappropriate dust climatology, but also due to missing physical processes in the model. Since then, the GCM has been improved, with a semi-interactive dust cycle to represent the dust vertical distribution and the inclusion of the radiative effect of water ice clouds (Madeleine et al., 2011, 2012; Navarro et al., 2014). Combined with an improved dust climatology, this has allowed a much better model-data agreement and thus a better understanding of the seasonal variation of the atmospheric density observed by SPICAM as shown in Fig. 13. SPICAM density and pressure variation measurements have also been used to detect and characterize non-migrating tides in the 70–120 km region by Withers et al. (2011). They found that the signal is dominated by wave-2 and wave-3 components and that they mostly result from the diurnal Kelvin waves 1 and 2.

Temperature profiles have been derived from the density profiles assuming that the atmosphere is in hydrostatic equilibrium (Quémerais et al., 2006; Montmessin et al., 2006b). The SPICAM measurements revealed interesting, but limited seasonal variations at a given pressure level, but large day-to-day and longitudinal fluctuations. The diurnal cycle could not be analyzed in detail because most data were obtained at nighttime, except for a few occultations observed around noon during northern winter. There, the averaged midday profile was found to differ slightly from the corresponding midnight profile, with the observed differences being consistent with propagating thermal tides and variations in local solar heating.

About 6% of the observed mesopause temperatures in MY27 exhibited temperature below the CO_2 frost point, especially
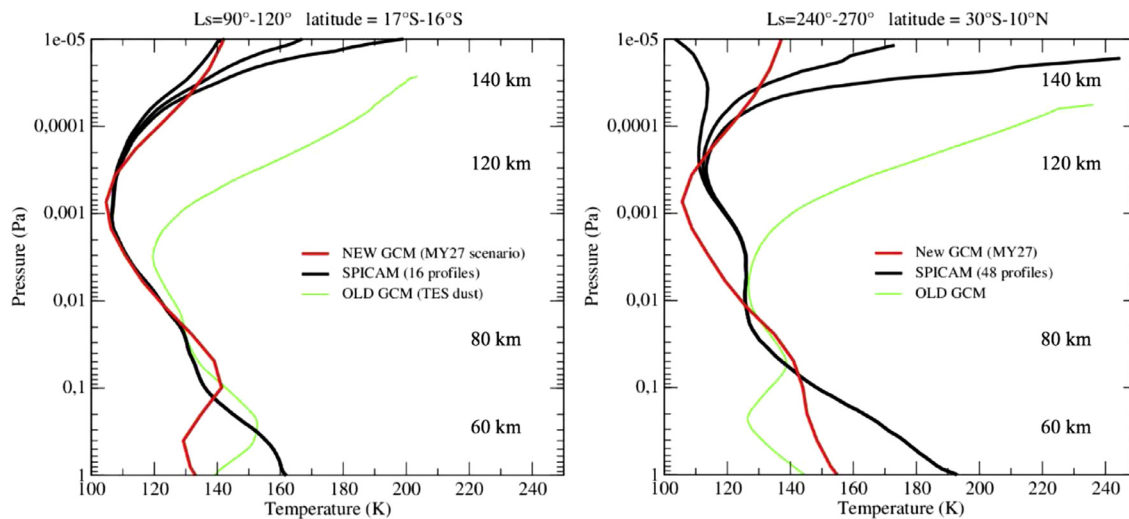
Fig. 14. Average temperature profiles measured by SPICAM (black lines), simulated by the version of the LMD-MGCM described in Forget et al. (2009) (green lines) and by the improved version of the model (red lines, see González-Galindo et al., 2013). The observations are averages of 16 profiles obtained between Ls = 90°–120° and latitude 17°S–16°S (left panel) and of 48 profiles obtained between Ls = 240° and 270° and latitude between 30S and 10 N (right panel). The modeled profiles are temporal and geographical averages for the same temporal and geographical intervals. Note that SPICAM temperatures below the 0.1 Pa level are thought to be overestimated. Approximate altitudes are given for reference. (For interpretation of the references to color in this figure legend, the reader is referred to the web version of this article).

during Northern summer in the tropics. The very high levels of supersaturation encountered suggest that CO_2 ice clouds similar to the one directly observed during the day by near-infrared imaging (Montmessin et al., 2007; Määttänen et al., 2010) may also form at night. Montmessin et al. (2006b) analyzed four examples of SPICAM stellar occultation observations of unusual detached aerosol layers around 100 km, thought to be clouds, and found that in each cases the simultaneous temperature measurements indicated subfreezing temperature a few kilometers above.

SPICAM temperature measurements have provided a first-hand validation for the thermospheric models. As detailed in Forget et al. (2009) and Gonzalez-Galindo et al. (2009) for the LMD GCM, as well as McDunn et al. (2010) for the Mars Thermosphere GCM developed at the University of Michigan, it was found that models strongly overestimated temperatures, i.e. the mesopause was found at too low altitudes. This discrepancy was analyzed and attributed to the parameterization of the cooling due to CO_2 15 μm emissions in Non-Local Thermal Equilibrium conditions as the likely responsible. For instance, the parameterizations used at LMD included a number of simplifications that affected the radiative transfer, and made use of a fixed, constant and uniform atomic oxygen concentration. Motivated by the SPICAM data, an improved parameterization has been developed to overcome those limitations (see López-Valverde et al., 2011 and González-Galindo et al., 2013) and the actual atomic oxygen profile calculated by the model is now taken into account. Fig. 14 shows two average SPICAM temperature profiles obtained at different seasons and latitudes, compared to the average temperature profiles predicted by the old version of the LMD GCM (and as shown in Forget et al., 2009, Fig. 15) and by the updated version of the model. The agreement is much better.

4.2. Ground-state molecular oxygen O_2

Understanding the distribution of ground-state O_2, a primary photochemical product on Mars, is important in constraining photochemical, dynamical and evolutionary models of the Martian atmosphere. For some reason, Sandel et al. (2015) have reported altitude profiles of O_2 from SPICAM UV observations of six stellar occultations. They inferred the O_2 abundance from absorption by O_2 in the Schumann–Runge continuum, which lies shortward of 175 nm. Although the absorption cross-section of O_2 is larger
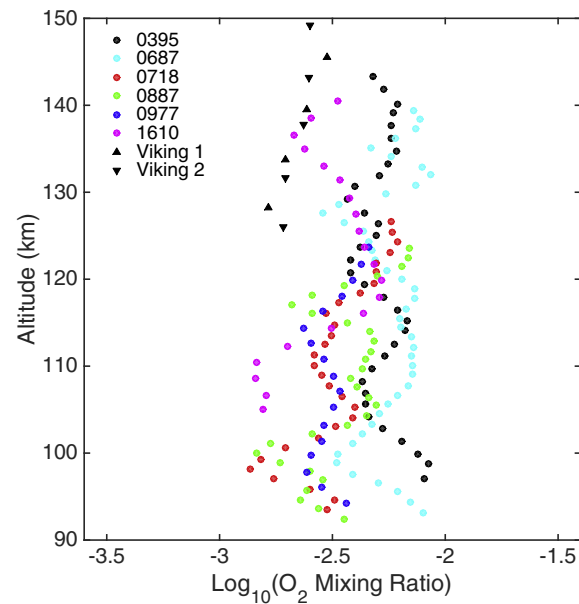

Fig. 15. The circles mark O_2 mixing ratios inferred from six UV stellar occultations (Sandel et al., 2015 for orbits/Ls of 0395/32,7°, 0687/68.9°, 0718/78.7°, 0887/93.5°, 0977/104.7°, 1610/195.4°). Error bars are omitted for clarity; typical values are in the range 10–25%. The numbers in the legend are the Mars Express orbit numbers. Geometry information about the sampled regions may be found in Table 2. The triangles indicate values from the lower part of the altitude range sampled by Viking. These profiles suggest variations in O_2 mixing ratio in space and time.

than that of CO_2 over much of the wavelength range of interest, the low mixing ratio of O_2 relative to CO_2 means that the O_2 absorption signature is at best a small feature in an absorption spectrum dominated by CO_2. This O_2 absorption signature was reliably measured and O_2 abundances inferred over an altitude range that varied among occultations, typically from 90 to 130 km, which spans much of the region of most active photochemistry. CO_2 abundances determined simultaneously from the same observations permit computing the O_2 mixing ratios, which are listed in Table 2 and plotted in Fig. 15. These mixing ratios are generally larger by a factor of three to four than values found for

Table 2

Characteristics of the observations used by Sandel et al. (2015) to infer the concentration of molecular oxygen in a fundamental state.

Time	Orbit	Lat (°)	LST (h)	L_s (°)	O_2 vmr[a],[b]
2004-05-13/10:34	0395	16.7	21.05	32.7	5.3 ± 1.1
2004-08-03/02:49	0687	−38.0	18.67	68.9	5.8 ± 1.5
2004-08-11/20:14	0718	−75.4	7.29	72.7	3.2 ± 1.1
2004-09-28/04:56	0887	−75.1	3.77	93.5	3.6 ± 1.3
2004-10-23/06:22	0977	−16.4	3.74	104.7	3.1 ± 0.6
2005-04-18/13:54	1610	37.7	21.99	195.4	3.3 ± 1.8

[a] Volume mixing ratio in units of 10^{-3}.
[b] Uncertainty reflects variation over altitude, not measurement uncertainty.

the lower atmosphere (see e.g. Owen et al., 1977; Hartogh et al., 2010; Mahaffy et al., 2013), but the lower SPICAM profiles are similar to those measured by Viking (Nier and McElroy, 1977) at similar altitudes. As a non-condensible species, O_2 located close to the surface of Mars is expected to exhibit seasonal variability caused by enrichment/depletion of non-condensible species subsequent to CO_2 freeze/thaw cycle. Our limited dataset does not allow us to conclude on a propagation of this seasonal signature at the altitudes where it is possible for SPICAM to detect O_2.

4.3. $O_2(a^1\Delta_g)$ nightglow

The $O_2(a^1\Delta_g)$ nightglow at 1.27 μm is a sensitive tracer of the middle and upper atmosphere circulation. Unlike the $O_2(a^1\Delta_g)$ dayglow emission that results from the O_3 photolysis (see also Guslyakova et al., 2014, 2016), the $O_2(a^1\Delta_g)$ nightglow is a product of the recombination of O atoms formed by CO_2 photolysis at altitudes higher than 80 km and transported to the winter pole by the Hadley circulation. The first detections of the $O_2(a^1\Delta_g)$ nightglow by OMEGA and CRISM showed that it is two order of magnitude less intense emission than the $O_2(a^1\Delta_g)$ dayglow (Bertaux et al., 2012; Clancy et al., 2012). In 2010 the vertical profiles of the $O_2(a^1\Delta_g)$ night side emission were obtained with SPICAM near the south pole at latitudes of 82–83°S for two sequences of observations: $L_s = 111°–120°$ and $L_s = 152°–165°$ (Fedorova et al., 2012). The altitude of the slant emission maximum observed by SPICAM varies from 45 km at $L_s = 111°–120°$ to 38–49 km at $L_s = 152–165°$. Once converted into a vertically integrated intensity, the emission at these latitudes shows an increase from 0.22 to 0.35 MR. Those values are consistent with the OMEGA observations reported in Bertaux et al. (2012). From the $O_2(a^1\Delta_g)$ nightglow it is possible to estimate the density of oxygen atoms at altitudes from 50 to 65 km, which is found to vary from 1.5×10^{11} to 2.5×10^{11} cm^{-3}. Comparison with the LMD GCM with photochemistry (Lefèvre et al., 2004, 2008) shows that the model reproduces fairly well the $O_2(a^1\Delta_g)$ emission layer observed by SPICAM at night, provided that the intrinsic vertical resolution (> 20 km on the limb) of the instrument is taken into account.

Since 2011 SPICAM IR has been carrying out a campaign at the northern and southern polar latitudes, where about 120 vertical profiles of the $O_2(a^1\Delta_g)$ nightglow have been obtained. The comparison of the emission detected in both polar regions shows that the emission peak is located at 35–42 km above the north pole versus 40–55 km above the south pole (see Fig. 16). The vertically integrated emission rate is about two times smaller than calculated by the LMD GCM. This difference may reflect the current uncertainties in the kinetics of the production of $O_2(a^1\Delta_g)$, or can be due to an inaccurate downward transport of O atoms by the GCM in the polar night region.

4.4. Nitric oxide (NO) nightglow

In the upper atmosphere of Mars, CO_2 and N_2 molecules are photodissociated by solar UV and EUV radiation. O and N atoms are then transported by the mean meridional circulation to the winter pole region. They recombine in the polar night as air parcels subside to form O_2 and NO (nitric oxide) molecules, as revealed by their nightglow emission at 1.27 μm and in the UV, respectively. Therefore, the NO UV nightglow emission in the δ (190–240 nm) and γ (225–270 nm) bands, which arises from radiative recombination between $O(^3P)$ and $N(^4S)$ forming excited NO molecules, is a good tracer of the dynamics of the Martian polar night between 30 km and 100 km. Following the discovery by SPICAM of the NO nightglow (Bertaux et al., 2005b), Cox et al. (2008) later analyzed 21 orbits of SPICAM containing limb observations of these NO UV emissions. This allowed an extensive description of the variability of the NO emission brightness peak and its peak altitude, mainly depending on the latitude and the season. The upper panel in Fig. 17 illustrates an example of an NO emission limb profile. From the comparison with a one-dimensional chemical-diffusive model, values for the oxygen and nitrogen density profiles (middle panel) and the eddy diffusion coefficient (lower panel) have been determined (Cox et al., 2008). The downward flux of N atoms at 100 km varies by two orders of magnitude, ranging from 10^7 to 10^9 atoms cm^{-2} s^{-1}. Oxygen and nitrogen density profiles present a peak near 50 km and 70 km. Cox et al. (2008) adopted an altitude dependence $K(z) = A / N^{1/2}$, where N is the total number density in cm^{-3} and A is a constant best fitting the observed limb profile. They found A values in the range 6.4×10^5 to 1.5×10^6, corresponding to K values about an order of magnitude less than other values in the literature.

To the above-mentioned dedicated limb data set was added a large number of stellar occultations, from which the NO signal was extracted for 128 occultations (Gagné et al., 2013). Overall, the SPICAM data cover almost three Martian years from $L_s = 44°$ of MY 27 to $L_s = 326°$ of MY 29 (Fig. 18). Around the southern winter solstice, all positive NO detections between $L_s = 60°$ and $L_s = 120°$ are at latitudes southward of 30°S. This is in agreement with the LMD GCM calculations, which show a strong NO emission in the descending branch of the Hadley circulation above the southern polar region. In contrast, around the northern winter solstice ($L_s = 240°–300°$), the SPICAM detections of NO are spread over a large latitude range, from 20°S to 70°N, whereas the LMD GCM predicts a much weaker emission near the equator than at high northern latitudes. Another North-South asymmetry is that the SPICAM "NO polar season" appears to be much shorter for the southern hemisphere than for the northern hemisphere. This is unexpected since the southern winter is longer than the northern winter, due to orbit eccentricity. For equinox conditions (around $L_s = 0°$ and $L_s = 180°$), SPICAM does not detect bright NO emissions poleward of 60°, contrary to the simultaneous NO maxima calculated by the LMD GCM above the poles in both descending branches of the Hadley circulation. These discrepancies between SPICAM data and current model calculations of the NO emission are still not understood.

A comprehensive survey of the SPICAM relevant database for NO (i.e. stellar occultations and limb observations) was conducted by Stiepen et al. (2015b) to further characterize the factors that control the NO nightglow emission layer. Out of a total of 5000 observations, NO nightglow was detected in 200 of them. They confirmed preliminary results by Cox et al. (2008) and Gagné et al. (2013) regarding the emission peak altitude (72 ± 10.4 km) and brightness (5 ± 4.5 kR). They showed that the large NO nightglow layer, from 42 to 97 km, experiences large brightness variability, ranging from 0.23 to 18.51 kR. Stiepen et al. (2015b) showed that the number of detections increases with higher solar activity. Yet, the solar activity does not play a role in the NO nightglow layer
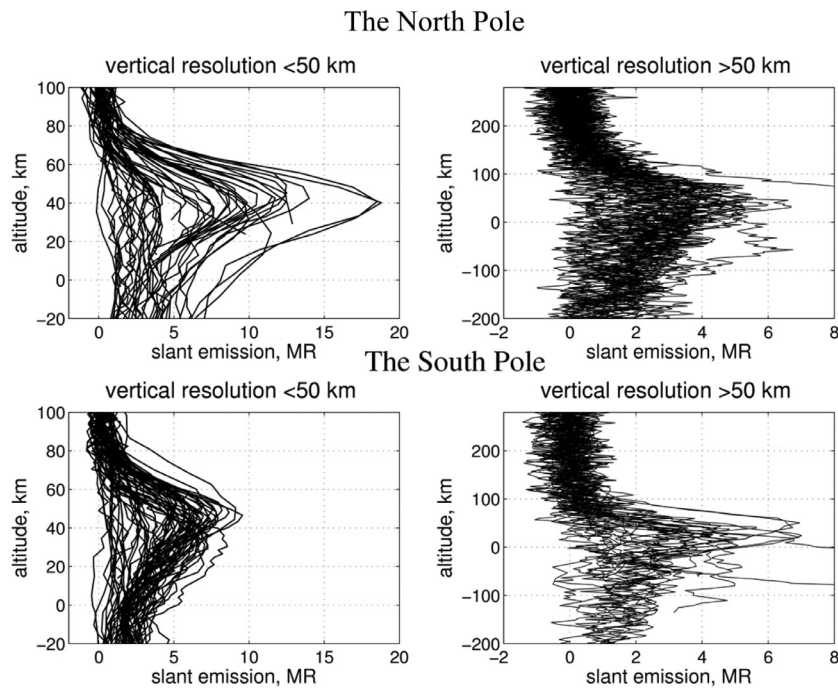
The North Pole

Fig. 16. Vertical profiles of the O2 nightglow expressed in MegaRayleigh (MR) in the south and north poles. Two kind of measurements are displayed: on the left, only the profiles collected with a vertical resolution smaller than 50 km, and on the right, the profiles assembled with a vertical resolution greater than 50 km, the latter inducing a noticeable reduction of the observed peak intensity.
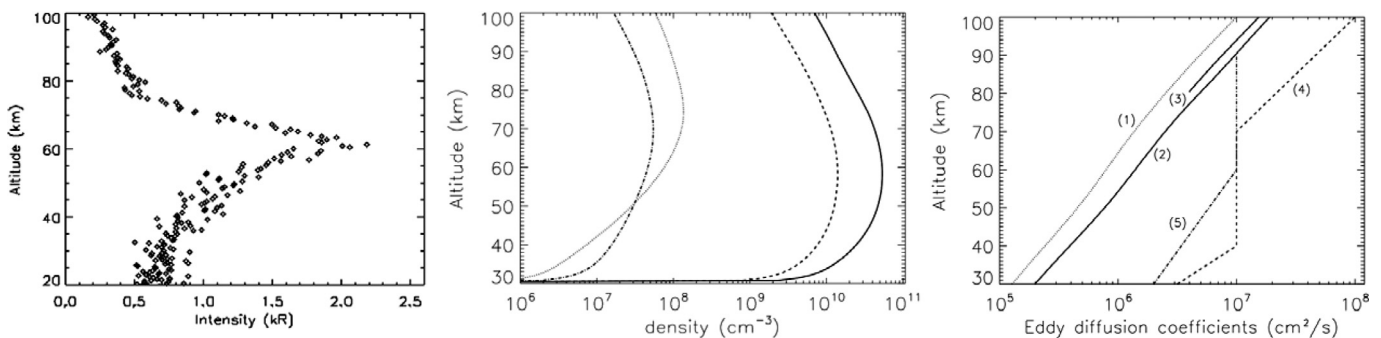

Fig. 17. (Adapted from Cox et al., 2008). Left: Limb profiles of the NO nightglow emission observed by SPICAM ; Middle : Atomic oxygen and nitrogen density profiles derived from 1-D model fits to the NO airglow observations. The solid and the dotted lines are respectively the O and N(4S) density profiles from orbit 716. The dashed and dotted-dashed lines are O and N from orbit 1577 respectively. Right : Estimates of the altitude variation of the eddy diffusion coefficient. Curve (1) is derived from the model fit to the limb profile of orbit 1577, (2) from the fit of the profile for orbit 716. (3) is the K(z) dependence adopted by Krasnopolsky (2002) while (4) and (5) are, respectively, the values used by Nair et al. (1994) and Krasnopolsky (2006) in their models of the Martian photochemistry.

altitude and brightness, an unexpected result that is still not understood. Stiepen et al. (2015b) constructed seasonal maps of the NO nightglow brightness and confirmed the data-model discrepancies found by Gagné et al. (2013) on a larger dataset.

These studies show the complexity of the path N and O atoms follow from the dayside thermosphere where they are created to the nightside mesosphere, where most recombine to form NO. The atoms cross a vertical section of ∼100 km and the NO nightglow emission is thus controlled by changes in this large section of the Martian atmosphere.

5. Upper atmosphere sounding (150 km to > 1000 km)

5.1. Exospheric hydrogen

The first observations of Lyman-α by SPICAM were obtained at Ls = 180° for solar moderate conditions (F10.7 at 1UA ∼100; Chaufray et al., 2008). Two kinds of observations were studied: four observations above the south pole and two observations near

the equator at SZA = 30° It was showed that one thermal hydrogen component with an exobase temperature equal to ∼200–250 K and an hydrogen density at the exobase of $1-2 \times 10^5$ cm^{-3} give a reasonable good fit to the observations, requiring however a scaling factor on the absolute brightness of ∼+ 10%. A better fit was obtained with the addition of a hot hydrogen population without scaling the absolute brightness for the observations at SZA=30° while the observations above south pole could be fitted by one thermal population with a temperature within 270–390 K. Simulations with a coupled three-dimensional atmosphere-exosphere model (Chaufray et al., 2017, submitted for publication) for solar average conditions (F10.7 = 118.3), at Ls = 150° – 180° are compared to these two kinds of observations in Fig. 19. The modeled Lyman-α brightness is overestimated for the observation at SZA=30°, implying an overestimated hydrogen density by the model. The model is in better agreement with the observations above the south pole especially if the measured brightness is rescaled by 10% but the scale height is slightly underestimated, which could be due to the presence of a hot hydrogen population.
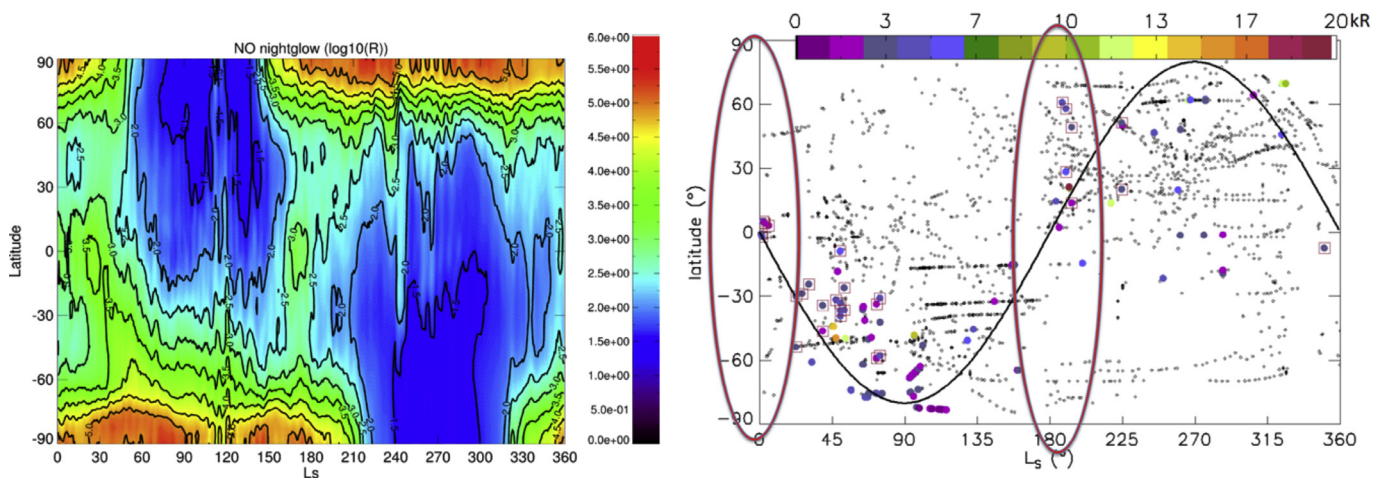
Fig. 18. (Upper plot) Zonal mean NO nightglow limb integrated intensity (Rayleigh) predicted by the LMD/MGCM (Gonzalez-Galindo et al., 2009) as a function of latitude and Ls at LT=21. Note that the color scale is logarithmic (3 covers 10^3 R). (Lower plot) NO observations plotted as a function of Ls and latitude. Color dots overlaid with squares represent time and location of the positive detections during that interval, with the color coding the measured limb intensity in kR. Color dots overlaid with squares represent the time, location, and intensity of dedicated limb intensities extracted from Cox et al. (2008). The black solid line is a sine curve, latitude $=-80 \times \sin$ (Ls), along which fall (more or less) the positive NO detections of both datasets, this one and that of Cox et al. (2008). Ellipses point to the solstice seasons. (For interpretation of the references to color in this figure legend, the reader is referred to the web version of this article).
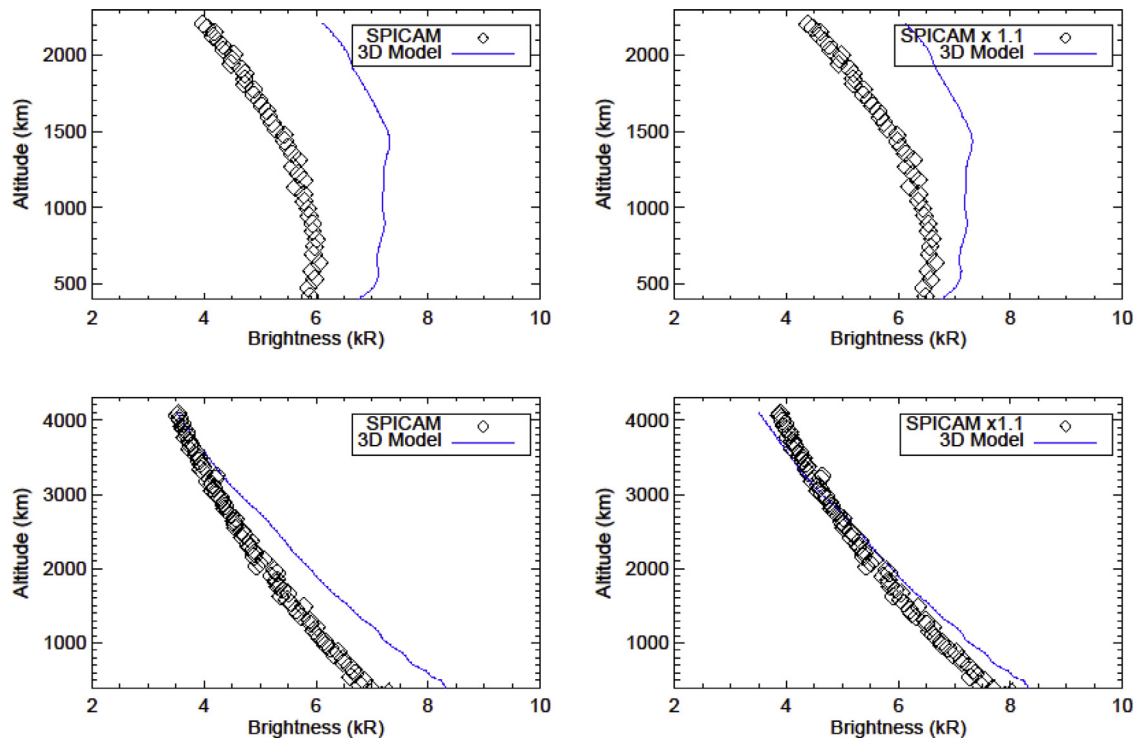

Fig. 19. H Lyman-α brightness as a function of altitude above the Martian limb observed by SPICAM/MEX during orbit 1541 (top) and 1514 (bottom) described in Chaufray et al. (2008) using the nominal calibration (left) and using a 10% rescaled brightness (right). The 3D model shown is described in Chaufray et al. (2013).

While a hot hydrogen component is unambiguous at Venus (Anderson, 1976), its detection at Mars has been more elusive due to the lower gravity of the planet and thus the more extended nature of the thermal corona. The source of hot hydrogen at Mars is unknown. Presumably, the same mechanisms that operate at Venus to produce a hot corona are active at Mars, but to date theoretical studies have indicated that hot H makes a very small contribution to the total H present in the corona (Nagy et al., 1990), a conclusion with which Chaufray et al. (2017) submitted for publication results apparently disagree.

Since the work of Hunten and McElroy (1970), photochemical models of the Martian atmosphere have predicted a $\sim 10^4$–10^5 year

timescale for the production of molecular hydrogen from water in the lower atmosphere. This molecular hydrogen is converted into atomic hydrogen in the ionosphere and provides what is thought to be the major source of the atomic hydrogen that escapes to space. Because the H_2 production timescale is much longer than the seasons and solar cycle, models predict that the H escape rate should not vary month-to-month or year-to-year. Contradicting this, Chaffin et al. (2014) demonstrated that in 2007, SPICAM-gathered altitude profiles of Lyman-α sunlight scattered from exospheric hydrogen imply an order-of-magnitude decline in the H escape rate, from previously unobserved levels. This likely represents relaxation from a temporarily enhanced escape rate, possibly due
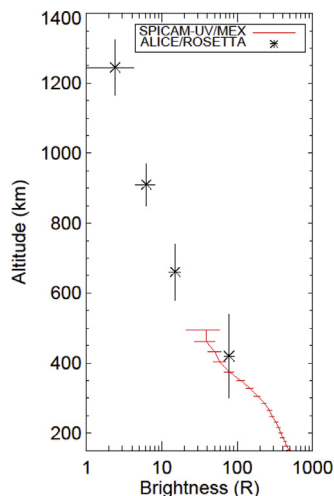
Fig. 20. O I 130.4 nm brightness derived from SPICAM/Mars Express (red line) and ALICE/Rosetta (black stars) as a function of altitude above the Martian limb. Adapted from Feldman et al. (2011). (For interpretation of the references to color in this figure legend, the reader is referred to the web version of this article).

to a global dust storm in which water was carried from the surface to the ionosphere, dramatically increasing atomic H production. These results show that H escape is more variable than previously suspected, potentially resulting in much larger integrated water loss over Martian history. Both simulations and observations are needed to understand and simulate properly the full cycle of the atomic hydrogen and its escape.

5.2. Exospheric oxygen

Atomic oxygen density in the Martian upper atmosphere can be constrained through the observations of its emission line at 130.4 nm. First observations performed by the Mariner missions concluded that two mechanisms were responsible of this emission: resonant scattering of solar photons and photoelectron impact excitation on atomic oxygen (Strickland et al., 1972, 1973; Fox and Dalgarno 1979; Stewart et al., 1992). The oxygen line was also observed by SPICAM UV. The analysis of the brightness vertical profiles (Fig. 20) performed by Chaufray et al. (2009) led to an estimate of the oxygen density at 200 km to be $\sim$1–2 $\times 10^7$ cm^{-3} at L_s $\sim$100°–160°, assuming an exobase temperature of 200 K. However, models with higher temperatures ($T \sim$300–340 K) led to a better fit. Chaufray et al. (2009) interpreted this as the effect of a nonnegligible contribution of the hot oxygen population between 300 and 400 km but no clear detection greater than 30 R of the hot oxygen corona could be retrieved from observations. ALICE/Rosetta as well as HST detected this hot oxygen corona and confirmed a low brightness of $\sim$10 R (Fig. 20) consistent with the SPICAM upper limit (Feldman et al. 2011; Carveth et al., 2013). Several studies have predicted the presence of a hot oxygen population dominant above 500 km. This hot oxygen corona originates mainly from the O_2^+ dissociative recombination (e.g. McElroy 1972; Nagy and Cravens, 1988; Chaufray et al., 2007; Valeille et al., 2009; Yagi et al., 2012). A thermal oxygen density of $\sim$3 $\times 10^7$ cm^{-3} at the exobase was found consistent with ALICE UV observations on Rosetta at Ls = 190° for low solar conditions (Feldman et al. 2011). This value as well as the brightness measurement near 400 km is in good agreement with SPICAM-UV measurements (Fig. 20).

The average dayside oxygen density at 200 km obtained with the LMD GCM (Yagi et al., 2012) at L_s = 120° – 150° for low solar conditions is $\sim$2.5 $\times 10^7$ cm^{-3} for an exospheric temperature of 190 K, in reasonable agreement with SPICAM observations The average oxygen density at 200 km increases by a factor of two
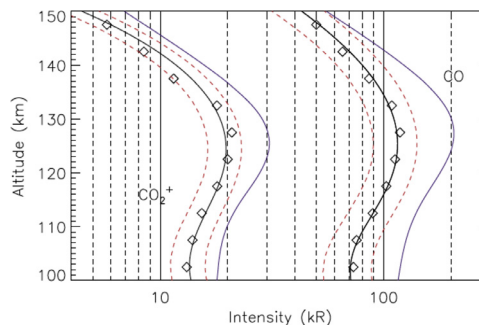

Fig. 21. Limb profiles of dayside airglow emissions observed with SPICAM (from Cox et al., 2010). The measurements (diamonds) of the CO Cameron and CO_2^+ doublet limb brightness have been binned into 5 km cells. The red dashed curves show the plus or minus 1 standard deviation. The blue curves were calculated with the dayglow model by Shematovich et al. (2008) for the same conditions as the observations. (For interpretation of the references to color in this figure legend, the reader is referred to the web version of this article).

from L_s = 90° to L_s = 150° consistent with an increase of a factor of about two derived from O I at 130.4 nm by Chaufray et al. (2009) from L_s = 100° to L_s = 160° This increase in oxygen density has been linked to a decrease of the altitude of the homopause by Gonzalez-Galindo et al. (2009), favoring the upward transport by molecular diffusion. Finally, the average oxygen density at 200 km decreases by $\sim$50% from 13HLT to 16HLT at this season, which is consistent with the decrease in oxygen density with solar zenithal angle derived by Chaufray et al. (2009). Therefore, the oxygen temporal trends derived from the LMD GCM model are consistent with the SPICAM observations at first order. Simulations of the oxygen brightness by a three-dimensional GCM-Exosphere model coupled to a radiative transfer model of the oxygen resonant line (Yagi et al., 2012) should be compared directly to the UV observations to provide a better quantification of the temporal trends.

5.3. Martian dayglow: CO Cameron bands and CO_2^+ doublet dayglow

SPICAM has provided extensive coverage of the CO and CO_2^+ ultraviolet dayglow. Limb profiles of the main emissions have been collected, covering a wide range of latitude and seasons. Leblanc et al. (2006a, 2007) and later Stiepen et al. (2015a) derived thermospheric temperatures from the scale height of the emission limb profiles. They found values ranging from 193 to 214 K, somewhat lower than predicted by the Mars GCM of Bougher et al. (2000). The exospheric temperature appeared largely independent of the solar zenith angle and season. Cox et al. (2010) also concluded that the occurrence of a major dust storm in 2007 modified the airglow emission profile, suggesting that the thermal perturbation propagates up to the thermosphere.

Cox et al. (2010) analyzed a set of 33 limb profiles of the CO ($a^3\Pi$ – $X^1\Sigma^+$) Cameron bands and CO_2^+ doublet at 298 and 299 nm (see Fig. 21). The data were collected during the spring season (L_s = 90–180°) between 100 and 150 km. They found that the average peak altitude of the Cameron band is 121.1 $\pm$ 6.5 km. They showed that the intensity is mainly controlled by the solar zenith angle and by solar activity, whereas the peak altitude seems to be dependent on the local CO_2 density profiles. They found good agreement between the measured limb profiles and those calculated with the one-dimensional model by Shematovich et al. (2008). They showed that the intensity of the peak emissions may be reproduced by introducing a scaling factor in the excitation cross sections. A similar conclusion was reached by Simon et al. (2009), Jain and Bhardwaj (2012) and Gronoff et al. (2012). It was estimated that Cameron band intensities calculated with the currently available cross sections are too large by a factor of two.

SPICAM dayglow spectra also made it possible to first identify the presence of the N_2 Vegard–Kaplan bands (Leblanc et al., 2007). The intensity distribution of this emission was recently modeled and reproduced by Jain and Bardwhaj (2011) and Fox and Hac (2013). The latter found that the predicted limb intensities are fully consistent with those observed by SPICAM.

5.4. Discovery of auroral activity on Mars

One of the first outstanding findings of SPICAM concerned the detection of auroral emissions (Bertaux et al., 2005a). They were called auroral emissions for basically three reasons: first, these faint and night side emissions are characterized by a sudden increase of intensity, from a few up to 30 seconds (see Figs. 1 and 2 of Bertaux et al., 2005a). Then, the processed spectrum contains dayglow features. Finally, the location of these emissions is remarkably connected to crustal magnetic anomalies. This kind of emissions corresponds to a distinct type of aurora not seen before in the Solar System: it is unlike aurorae at Earth and the giant planets, which lie at the foot of the intrinsic magnetic field lines near the magnetic poles, and unlike Venusian atomic oxygen auroras, which are diffuse, sometimes spreading over the entire disk. Instead, this aurora identified on Mars is a highly concentrated and localized emission due to energetic electrons channeled by magnetic field anomalies, which impact the atmosphere with an energy distribution peaking at few tens of eV (Leblanc et al., 2006b). Auroras have been detected in all seasons. The intensities range from 100 to 2000 R for the CO Cameron bands and from 10 to 160 R for the CO_2^+ doublet. The altitude of the emission is around 130 km. The signature of the auroral processes has also been recorded in the ASPERA-3/Electron Spectrometer data and in the Total Electron Content derived from the MARSIS radar (Leblanc et al., 2008). Since then, new types of auroras have been detected by the IUVS instrument onboard MAVEN, suggesting more widespread occurrences with increased solar activity (Schneider et al., 2015).

The SPICAM nightglow database collected over 10 years in the nadir direction was searched by Gérard et al. (2015) who analyzed a total of 16 auroral UV events together with concurrent measurements of energetic electrons made with the ASPERA-3/ELS. They confirmed the close association with regions located near the open-closed magnetic field line boundary in cusp-like structures. This concluded the Martian aurora is an infrequent phenomenon, as a majority of the MEx passes over the "auroral" regions at different times and dates showed no signature of UV auroral events. Soret et al. (2016) focused on three limb observations to quantify the altitude of the aurora. They found that the auroral emissions are strongly confined in size and they estimated the peak altitude of the CO Cameron bands to be 137 ± 27 km. Using electron energy spectra measured with the ASPERA-3/ELS instrument, they calculated altitudes with a Monte Carlo electron transport code in very good agreement with the observations, but found strong discrepancies between the predicted and observed nadir intensities.

6. Conclusion

During the past 10 years, the SPICAM instrument onboard Mars Express has contributed to the improvement of the understanding of Mars' climate in several areas, including lower atmosphere composition and chemical processes, lower atmosphere structure and its governing dynamical processes, up to the thermosphere and above where atomic species like oxygen and hydrogen have been characterized. Mars' climate is the complex result of a variety of "agents" interacting together: dust, water ice clouds and vapor, carbon dioxide. SPICAM has enabled detailed investigation of these

interactions in a unique way as it combines the possibility to monitor all these species simultaneously and to provide constraints on both their horizontal and their vertical distribution.

On the basis of the results collected to date, it is possible to draw a common thread to the variety of topics covered by the instrument. The nadir observation mode has produced one of the longest climatology published to date for both of water vapor (IR) and ozone (UV) column abundances, confirming their suspected anti-correlation. This is controlled by the release of H, OH and HO_2 radicals from the decomposition of water vapor, these radicals being powerful destroyers of odd oxygen O and O_3. In parallel, SPICAM IR in solar occultation mode has established a detailed characterization of the H_2O vertical distribution, revealing a salient feature for water vapor that was not anticipated: the presence of unexpected amounts of water vapor above 30 km where it can be photodissociated into H and OH. While it has been proposed (Maltagliati et al., 2011) and later modeled (Navarro et al., 2014) that the presence of water in excess of saturation above the cloud layer during the Aphelion season is likely caused by cloud formation processes impeded by the lack of condensation nuclei, the presence of water vapor above 40 km up to concentrations exceeding 100 ppm (Maltagliati et al., 2013) remains to be understood and explained by models.

These large amounts of water vapor exposed to UV sunlight at such altitude become quickly photodissociated and a local production of hydrogen atoms in the mesosphere provides an access to the exobase more straightforward than previously theorized. The direct deposition of hydrogen atoms in the upper mesosphere and further transportation in the lower thermosphere is supported by the recent discovery of a polar ozone layer at the winter south pole, indicative of planetary-scale transport and recombination of oxygen atoms from the summer hemisphere during solstice. The absence of a comparable layer at the north pole during the corresponding winter season in the northern hemisphere has been explained by three-dimensional chemistry models to result from the equator-to-pole advection of hydrogen atoms produced in the summer southern mid-latitudes, where SPICAM IR revealed water-vapor rich layers above 60 km.

Finally, the seasonal evolution of hydrogen, which can be observed and characterized above the exobase from limb staring Lyman-alpha modes (Chaffin et al., 2014), has revealed a behavior of hydrogen atoms contradicting the canonical view of an upper reservoir of H seasonally disconnected from its water vapor precursor in the lowest atmospheric layers. The timescale of $\sim 10^4–10^5$ years predicted by models for the conversion of water to escaping hydrogen is the result of chemical reactions at high altitude involving dissociative ionization of H_2 mainly by CO_2^+ (Hunten and McElroy, 1970; Krasnopolsky et al., 2002). As shown by Chaffin et al. (2014) with SPICAM and by Clarke et al. (2014) from Hubble Space Telescope observations, the hydrogen corona shows puzzling variations over short term (e.g. months) that appears to be correlated with lower atmosphere variability.

• Mars atmosphere: a highway to space for hydrogen?

From this ensemble of results, we can infer that the communication between the well-mixed lower atmosphere and the outer layers where atoms (hydrogen in particular) can freely escape is more direct and much faster than anticipated. Escape processes for water need to be reappraised in light of this consideration. The Martian atmosphere appears as one single coherent system, able to react on short timescales and which may therefore have been dominated throughout its history by seasonal peaks.

their support through contribution of human resources necessary for SPICAM operation planning and data analysis.

Appendix

The following provides a summary of the main changes regarding our understanding of the instrument characteristics since there were first presented with SPICAM in flight in Bertaux et al. (2006).

Instrument Point-Spread Function

• UV channel

Characterizing the detailed Point-Spread-Function (PSF) of the UV channel proved more complicated than initially understood and reported in previous works on the topic (Quémerais et al., 2006; Bertaux et al., 2006). While these early studies mention a 2–3 pixel-wide Gaussian shape as a best fit for the PSF, several stellar observations yielding transmission of the entire CCD frame without any binning have provided stronger constraints on the analytical form of the photon spread.

SPICAM UV PSF is actually best represented by a Voigt function (whose parameters are given in Fig. 4) and this implies the existence of a far-wing in the line profile that was previously ignored (Snow et al., 2013). This far-wing contribution is equivalent to a spread for a monochromatic point source covering a disk of > 40 pixel-diameter in the CCD plane. In practice, a cut-off at a distance of about 40 pixels from the center is added to avoid excessive redistribution of photon energy in the far wings. The exact value for the cut-off distance is not very well constrained, as the signal of the star used for this analysis beyond 20 pixels becomes dominated by noise. An alternative form, consisting of a linear combination of a Gaussian and a Lorentzian curve instead of their convolution, would offer more amplitude to redistribute energy between the core and the wings. In addition, it would reduce substantially the computational cost of the Voigt function. For these reasons, it is planned to implement this functional form in the future.

• Infrared channel

The IR channel's spectral response function is best described as $\sin^2 x/x^2$, and its FWHM of $\sim 3.5\,\text{cm}^{-1}$ is nearly constant in wavenumbers within the spectral range.

High voltage spike consideration and mitigation

A typical example of an observational sequence affected by these high voltage spikes is shown in Fig. 22. These spikes induce a temporary elevation/reduction of unknown amplitude of the intensifier gain. The consequence is the loss for the infected spectra of their calibration state making them impractical to scientific exploitation. Fortunately, the occurrence of these spikes is accompanied by distinct variations in the properties of the recorded spectra. To identify these spikes, we use the so-called "normalized cord length" (NCL) of the spectrum,

defined as

$$NCL = \frac{\sum_{i=1}^{n-1}\sqrt{(S_i - S_{i+1})^2 + 1}}{\sum_{i=1}^{n-1} S_i}$$

with S_i the readout of pixel #i (from 1 to 384). This expression gives a characterization of the relative noise amplitude in a complete spectrum. A NCL-based selection criterion actually provides an effective proxy to isolate infected spectra from unaffected ones. In a sequence of observation, the NCL of "healthy" spectra scatter around a constant value that lies statistically distant from the values of the infected spectra (see Fig. 22). This approach is however insufficient to capture all the spikes and the final selection process makes use of additional criteria, including the variability of the spectrum itself.

Straylight consideration and mitigation

Several types of stray light affect SPICAM measurements. Below is the up-to-date "taxonomy" of stray light(s) compiled for both channels. Note that stray light mitigation is not currently part of the processing leading to the production of Level 1A data (see below) that is freely accessible.

• UV Channel

One of the most important sources of stray light is caused by the far wing component of the instrument PSF. Referring to stray light may appear debatable in this specific case. However, we choose to refer to stray light regardless of its cause but only in regard of its consequence, that is causing the presence of undesired photons at any given position on the detector.

A first version of the treatment of stray light in nadir observations was designed and used in earlier analysis of SPICAM data (Bertaux et al., 2006; Perrier et al., 2006). This type of stray light is of "internal" type as all photons come from the observed scene. It is now understood after updating the PSF that this stray light is induced by the far wings of the scene illuminating the wide portion of the slit.

In the case the observed scene can be assumed fully uniform, the problem can be solved in two ways; either by implementing a two-dimensional Voigt convolution of the slit illumination in a forward modeling approach or by matrix inversion by pre-computing a dispersion matrix whose elements are defined by the assumed Voigt function. The most recent ozone retrieval, as presented later in the manuscript, has been performed with the former method. The proportion of stray light is wavelength dependent, accounting for 30% in the bright part of the solar spectrum and is the dominant signal on the edges.

In the case where the scene is not uniform across the slit, the problem becomes complicated since the slit illumination vector needs to be resolved as well. This kind of situation occurs typically while staring at the limb when the scene features large illumination gradient. No correction of this kind has ever been validated to date and the limb observations analyzed thus far have relied on empirical stray light subtraction (Leblanc et al., 2006a).

A different kind of stray light is identified during stellar occultation. This stray light is promoted by the absence of the slit, which is retracted at the beginning of the occultation sequence to compensate potential pointing variations and to avoid spurious stellar signal fluctuations. On the other hand, such configuration corresponds to 100 times increase of the aperture in the spectral direction, significantly increasing the chances of capturing signals other than the star itself. This case has been well documented with the SPICAV instrument around Venus (Royer et al., 2010; Piccialli et al., 2015) and a major "other" signal is produced by nitric oxide emission (NO) that is widespread on the night side of Venus. NO emission also exists on Mars and needs to be removed, yet appears less intense and less frequent than on Venus. For details regarding the
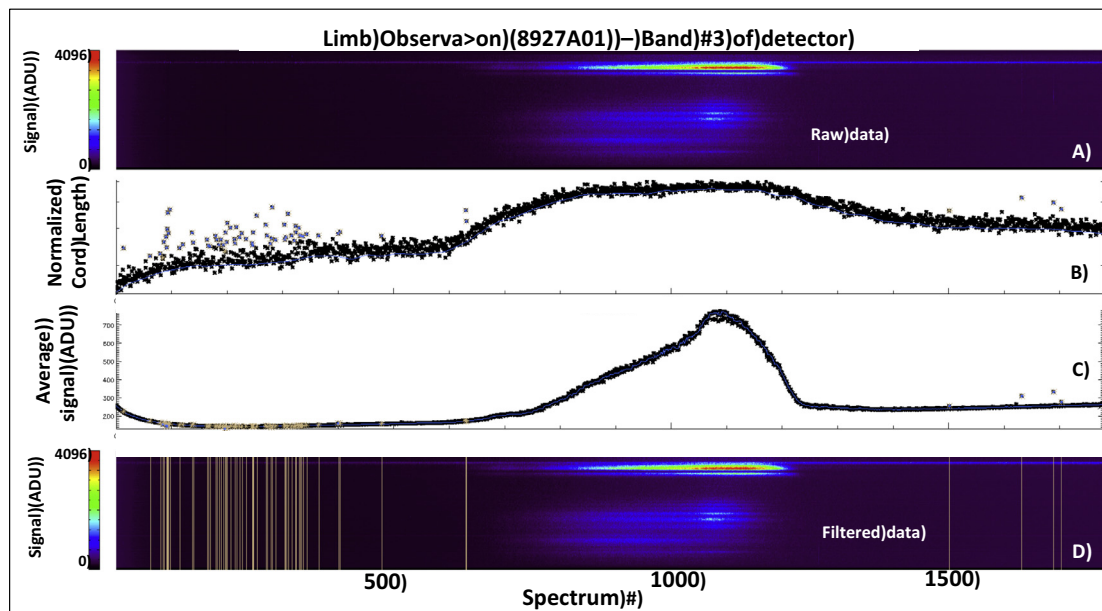
Fig. 22. An example of the data cleaning procedure to isolate and remove UV channel spectra affected by high voltage spikes. (A) Raw version of SPICAM UV data (Level 0) showing the evolution over time (30 min sequence composed of 1 spectrum / second) of the spectra collected by the instrument. The wavelength axis is placed along the vertical of the image and signatures of NO emission around record #1000 are present. (B) The related normalized cord length (see text for formula). The presence of HV spikes is delineated by the outliers. (C) Average signal (all wavelength summed together) with time, the presence of HV spikes is not easily identified with such representation. (D) Cleaned version of (A) – Level 1A of SPICAM UV data where HV spikes have been flagged and removed from further analysis.

NO emission subtraction procedure, the reader is referred to Royer et al. (2010).

• Infrared Channel

The issue of the straylight in the AOTF, or the distant side lobes of its spectral response function (SRF) has been raised because early SPICAM water vapor retrievals have been found generally to be lower than simultaneous measurements obtained with other Mars Express instruments. Stray light or spectral leakage was suggested as a likely explanation. When the RF is turned off, the AOTF serves as an electronic shutter, allowing accurate subtraction of the background signal, measured after every measurement. The synchronous modulation cancels out all the stray light, which is not the result of the acousto-optic interaction. However, scattering or multiple reflections of the acoustic wave field inside the crystal may be generated by imperfect coupling of the transducer to the crystal or imperfect absorber. The optical diffraction of this spurious field produces a synchronous parasitic signal. Possible reasons for the stray light in the SPICAM infrared channel are detailed in Korablev et al. (2006a).

The transmission spectrum of the 1.38-μm water vapor band looks like a continuum with weak gaseous absorption features. The spectral leakage results in the increase of the measured continuum, while the depth of the measured absorption features remains nearly the same. Then the apparent equivalent optical depth (the optical depth integrated over the spectral interval of interest) decreases. With high resolving power ($\lambda/\Delta\lambda = 2000$) a small spectral leakage, e.g. of $\sim3 \times 10^{-4}$ may translate into a $\sim6\%$ error in the apparent equivalent optical depth.

In order to characterize the stray light, laboratory measurements of water vapor in quantity typical of the Mars atmosphere (2–15 pr μm) were performed with the flight spare model of SPICAM-IR. The measured spectra were simulated with a HITRAN-based synthetic model, varying the water abundance, the level of the stray light, and comparing the results to the known amount of water in the cell. The retrieved level of stray light, assumed uniformly spread over the spectral range is below 1–1.3×10^{-4}, as expected from a high-quality grating spectrometer. This stray light may lead to an underestimation of the water abundance of up to

8%, or 0.6 pr. μm. Taking into account the stray light in the retrieval algorithm removes completely the bias previously observed with respect to other Mars Express instruments, bringing the overall accuracy to measure water vapor to ~0.2 pr. μm (Korablev et al., 2013).

Higher level data production: dark charge and readout pattern removal

The highest level of data products (Level 1A data) currently accessible and deposited on the ESA Planetary Science Archive website incorporates a two-stage correction that consists in (1) subtracting the background signal generated by the CCD dark charge and (2) in removing the correlated readout pattern.

Estimation and correction of the dark charge for each observation is performed by making use of the signal recorded in the masked pixels located at the edge of each detector line of pixels. Dedicated sequences of observations with the intensifier inactive (effectively suppressing any photon input) have allowed the establishment of a statistically robust linear dependence between each pixel and its corresponding masked pixel. This law was then propagated to every sequence of observation with the intensifier activated. The derived dark charge pattern has been updated approximately once a month.

Readout pattern correlates pixel together and can be represented by a sine function superimposed on top of the recorded spectra. Its amplitude is generally equivalent to less than 1% of the brightest signals. However, readout bias may dominate over photon statistics at low counts. In most cases, observed sources only cover a portion of the available spectral range and a dark portion remains that permits to identify and isolate the readout pattern. The latter is usually well fitted by a sine function, whose parameters are determined by fitting the dark portion at every acquisition.

For stellar occultation, the spectrum covers the full available range and no dark spectral portion can be used. However, the bins adjacent to the main bin containing the stellar signal are usually free of any signal and readout pattern can be accessed this way. There is a phase correlation between the readout patterns of the five bins and this correlation can be established during the "blind" portion of the occultation, when the line of sight intersects the

dark side of the planet. Once this correlation between bins of pixels is obtained, it is extrapolated to the illuminated portion of the occultation and removed from the stellar signal.

In the IR channel, the instrument employs synchronous modulation (the AOTF is on during 50% of the measurement cycle), however a slightly variable temperature-dependent background, or dark current, originates from RF electrical interference. The removal of this background is described in Korablev et al. (2006a, 2006b).

References

Anderson, DonaldE., 1976. The mariner 5 ultraviolet photometer experiment: analysis of hydrogen lyman alpha data. J. Geophys. Res. 81 (7), 1213–1216. doi:10.1029/JA081i007p01213.

Barth, C.A., Hord, C.W., Stewart, A.I., Lane, A.L., Duck, M.L., Anderson, G.P., 1973. Mariner 9 ultraviolet spectrometer experiment: Seasonal variation of ozone on Mars. Science 179, 795–796.

Bertaux, J.-L., Leblanc, F., Witasse, O., Quemerais, E., Lilensten, J., Stern, S.A., Sandel, B., Korablev, O., 2005a. Discovery of an aurora on Mars. Nature 435, 790–794. doi:10.1038/nature03603.

Bertaux, J.-L., Leblanc, F., Perrier, S., Quemerais, E., Korablev, O., Dimarellis, E., Reberac, A., Forget, F., Simon, P.C., Stern, S.A., Sandel, B., 2005b. Nightglow in the upper atmosphere of Mars and implications for atmospheric transport. Science 307, 566.

Bertaux, J.-L., Korablev, O., Perrier, S., Quémerais, E., Montmessin, F., Leblanc, F., Lebonnois, S., Rannou, P., Lefèvre, F., Forget, F., Fedorova, A., Dimarellis, E., Reberac, A., Fonteyn, D., Chaufray, J.Y., Guibert, S., 2006. SPICAM on Mars Express: observing modes and overview of UV spectrometer data and scientific results. J. Geophys. Res. (Planets) 111, 10. doi:10.1029/2006JE002690.

Bertaux, J.L., Gondet, B., Lefèvre, F., Bibring, J.P., Montmessin, F., 2012. First detection of O₂ 1.27 μm nightglow emission at Mars with OMEGA/MEX and comparison with general circulation model predictions. J. Geophys. Res. (Planets) 117. doi:10.1029/2011JE003890.

Bibring, J.-P., 2005. Mars surface diversity as revealed by the OMEGA/Mars Express observations. Science 307, 1576–1581. doi:10.1126/science.1108806.

Bougher, S.W., Engel, S., Roble, R.G., Foster, B., 2000. Comparative terrestrial planet thermospheres: 3. Solar cycle variation of global structure and winds at solstices. J. Geophys. Res. 105, 17669–17689.

Böttger, H.M., et al., 2004. The effect of a global dust storm on simulations of the Martian water cycle. Geophy. Res. Lett. 31. doi:10.1029/2004GL021137.

Böttger, H.M., Lewis, S.R., Read, P.L., Forget, F., 2005. The effects of the martian regolith on GCM water cycle simulations. Icarus 177, 174–189. doi:10.1016/j.icarus.2005.02.024.

Carveth, C., Clarke, J., Chaufray, J-Y., Bertaux, J-L., 2013. Analysis of HST spatial profiles of oxygen airglow from Mars. Bull. Am. Astron. Soc. 44, 214 (abstract).

Chaffin, M.S., Chaufray, J.-Y., Stewart, I., Montmessin, F., Schneider, N.M., Bertaux, J.-L., 2014. Unexpected variability of Martian hydrogen escape. Geophys. Res. Lett. 41, 314–320. doi:10.1002/2013GL058578.

Chaufray, J.-Y., Modolo, R., Leblanc, F., Chanteur, G., Johnson, R.E., Luhmann, J.G., 2007. Mars solar wind interaction: formation of the Martian corona and atmospheric loss to space. J. Geophys. Res. 112, E09009. doi:10.1029/2007JE002915.

Chaufray, J.-Y., Bertaux, J.-L., Leblanc, F., Quémerais, E., 2008. Observation of the hydrogen corona with SPICAM on Mars Express. Icarus 195, 598–613.

Chaufray, J.-Y., Leblanc, F., Quémerais, E., Bertaux, J.-L., 2009. Martian oxygen density at the exobase deduced from OI 130.4 nm observations by SPICAM on Mars Express. J. Geophys. Res. 114, E02006. doi:10.1029/2008JE003130.

Clancy, R.T., et al., 2012. Extensive MRO CRISM observations of 1.27 μm O₂ airglow in Mars polar night and their comparison to MRO MCS temperature profiles and LMD GCM simulations. J. Geophys. Res. (Planets) 117. doi:10.1029/2011JE004018.

Clancy, R.T., Wolff, M.J., Lefèvre, F., Cantor, B.A., Malin, M.C., Smith, M.D., 2016. Daily global mapping of Mars ozone column with MARCI UV band imaging. Icarus.

Clancy, R.T., Grossman, A.W., Wolff, M.J., James, P.B., Rudy, D.J., Billawala, Y.N., Sandor, B.J., Lee, S.W., Muhleman, D.O., 1996. Water vapor saturation at low latitudes around aphelion: a key to Mars climate? Icarus 122, 36–62.

Clancy, R.T., Wolff, M.J., James, P.B., 1999. Minimal aerosol loading and global increases in atmospheric ozone during the 1996–1997 Martian northern spring season. Icarus 138, 49–63.

Clarke, J.T., Bertaux, J.-L., Chaufray, J.-Y., Gladstone, G.R., Quémerais, E., Wilson, J.K., Bhattacharyya, D., 2014. A rapid decrease of the hydrogen corona of Mars. Geophys. Res. Lett. 41, 8013–8020. doi:10.1002/ 2014GL061803.

Cox, C., Saglam, A., Gérard, J.-C., Bertaux, J.-L., Gonzalez-Galindo, F., Leblanc, F., Reberac, A., 2008. Distribution of the ultraviolet nitric oxide Martian night airglow: observations from Mars Express and comparisons with a one-dimensional model. J. Geophys. Res. (Planets) 113 (E8), E08012. doi:10.1029/2007JE003037.

Cox, C., Gérard, J.C., Hubert, B., Bertaux, J.L., Bougher, S.W., 2010. Mars ultraviolet dayglow variability: SPICAM observations and comparison with airglow model. J. Geophys. Res. 115, E04010. doi:10.1029/2009JE003504.

Encrenaz, T., Greathouse, T.K., Richter, M.J., Lacy, J.H., Fouchet, T., Bézard, B., Lefèvre, F., Forget, F., Atreya, S.K., 2011. A stringent upper limit to SO₂ in the Martian atmosphere. Astron. Astrophys. 530, A37. doi:10.1051/0004-6361/201116820.

Encrenaz, T., Melchiorri, R., Fouchet, T., Drossart, P., Lellouch, E., Gondet, B., Bibring, J.-P., Langevin, Y., Titov, D., Ignatiev, N., Forget, F., 2005. A mapping of martian water sublimation during early northern summer using OMEGA/Mars Express. Astron. Astrophys. 441, L9–L12. doi:10.1051/0004-6361:200500171.

Fast, K., Kostiuk, T., Hewagama, T., A'Hearn, M.F., Livengood, T.A., Lebonnois, S., Lefèvre, F., 2006. Ozone abundance on Mars from infrared heterodyne spectra. Icarus 183, 396–402. doi:10.1016/j.icarus.2006.03.012.

Fedorova, A., Korablev, O., Bertaux, J.L., Rodin, A., Kiselev, A., Perrier, S., 2006a. Mars water vapor abundance from SPICAM IR spectrometer: seasonal and geographic distributions. J. Geophys. Res. 111, E09S08. doi:10.1029/2006JE002695.

Fedorova, A., Korablev, O., Perrier, S., Bertaux, J.L., Lefevre, F., Rodin, A., 2006b. Observation of O₂ 1.27 μm dayglow by SPICAM IR: seasonal distribution for first Martian year of Mars-Express. J. Geophys. Res. 111, E09S07. doi:10.1029/2006JE002694.

Fedorova, A.A., Korablev, O.I., Bertaux, J.-L., Rodin, A.V., Montmessin, F., Belyaev, D.A., Reberac, A., 2009. Solar infrared occultation observations by SPICAM experiment on Mars-Express: simultaneous measurements of the vertical distributions of H₂O, CO₂ and aerosol. Icarus 200, 96–117. doi:10.1016/j.icarus.2008.11.006.

Fedorova, A.A., Trokhimovsky, S., Korablev, O., Montmessin, F., 2010. Viking observation of water vapor on Mars: revision from up-to-date spectroscopy and atmospheric models. Icarus 208, 156–164. doi:10.1016/j.icarus.2010.01.018.

Fedorova, A.A., Lefèvre, F., Guslyakova, S., Korablev, O., Bertaux, J.-L., Montmessin, F., Reberac, A., Gondet, B., 2012. The O₂ nightglow in the martian atmosphere by SPICAM onboard of Mars-Express. Icarus 219 (2), 596–608.

Fedorova, A.A., Montmessin, F., Rodin, A.V., Korablev, O.I., Määttänen, A., Maltagliati, L., Bertaux, J.-L., 2014. Evidence for a bimodal size distribution for the suspended aerosol particles on Mars. Icarus 231, 239–260. doi:10.1016/j.icarus.2013.12.015.

Feldman, P.D., et al., 2011. Rosetta-ALICE observations of exospheric hydrogen and oxygen on Mars. Icarus 214, 394–399.

Forget, F., Montmessin, F., Bertaux, J-L., Gonzalez-Galindo, F., Lebonnois, S., Quémerais, E., Réberac, A., Dimarellis, E., López-Valverde, M.A., 2009. Density and temperatures of the upper Martian atmosphere measured by stellar occultations with Mars Express SPICAM. J. Geophys. Res. 114, E01004. doi:10.1029/2008JE003086.

Formisano, V., et al., 2006. The planetary fourier spectrometer (PFS) onboard the European venus express mission. Planet. Space Sci. 54, 1298–1314. doi:10.1016/j.pss.2006.04.033.

Fouchet, T., Lellouch, E., Ignatiev, N.I., Forget, F., Titov, D.V., Tschimmel, M., Montmessin, F., Formisano, V., Giuranna, M., Maturilli, A., Encrenaz, T., 2007. Martian water vapor: Mars Express PFS/LW observations. Icarus 190, 32–49.

Fox, J.L., Dalgarno, A., 1979. Ionization, luminosity, and heating of the upper atmosphere of Mars. J. Geophys. Res. 84, 7315 1979.

Fox, J.L., Haĉ, N.E.F., 2013. Intensities of the Martian N₂ electron-impact excited dayglow emissions. Geophys. Res. Lett. 40, 2529–2533. doi:10.1002/grl.50435.

Gagné, Marie-Eve, Bertaux, J.-L., González-Galindo, F., Melo, S.M.L., Montmessin, F., Strong, K., 2013. New nitric oxide (NO) nightglow measurements with SPICAM/MEx as a tracer of Mars upper atmosphere circulation and comparison with LMD-MGCM model prediction: Evidence for asymmetric hemispheres. J. Geophys. Res. (Planets) 118, 2172–2179. doi:10.1002/jgre.20165.

Gérard, J.-C., Soret, L., Libert, L., Lundin, R., Stiepen, A., Radioti, A., Bertaux, J.-L., 2015. Concurrent observations of ultraviolet aurora and energetic electron precipitation with Mars Express. J. Geophys. Res. 120. doi:10.1002/2015JA021150.

González-Galindo, F., Forget, F., López-Valverde, M.A., Angelats i Coll, M., Millour, E., 2009. A ground-to-exosphere Martian general circulation model: 1. Seasonal, diurnal, and solar cycle variation of thermospheric temperatures. J. Geophys. Res. 114, E04001. doi:10.1029/2008JE003246.

González-Galindo, F., Chaufray, J.-Y., López-Valverde, M.A., Gilli, G., Forget, F., Leblanc, F., Modolo, R., Hess, S., Yagi, M., 2013. Three-dimensional Martian ionosphere model: I. The photochemical ionosphere below 180 km: 3D MARTIAN IONOSPHERE I. J. Geophys. Res. Planets 118, 2105–2123. doi:10.1002/jgre.20150.

Gronoff, G., Simon Wedlund, C., Mertens, C.J., Barthélemy, M., Lillis, R.J., Witasse, O., 2012. Computing uncertainties in ionosphere-airglow models: II. The Martian airglow. J. Geophys. Res. 117, A05309. doi:10.1029/2011JA017308.

Guslyakova, S., Fedorova, A.A., Lefèvre, F., Korablev, O.I., Montmessin, F., Bertaux, J.-L., 2014. O₂(a1△g) dayglow limb observations on Mars by SPICAM IR on Mars-Express and connection to water vapor distribution. Icarus 239, 131–140. doi:10.1016/j.icarus.2014.05.040.

Guslyakova, S., Fedorova, A., Lefèvre, F., Korablev, O., Montmessin, F., Trokhimovsky, A., Bertaux, J.-L., 2016. Long-term nadir observations of the O₂ dayglow by SPICAM IR. Planet. Space Sci. 122, 1–12. doi:10.1016/j.pss.2015.12.006.

Hartogh, P., et al., 2010. Herschel/HIFI observations of Mars: first detection of O₂ at submillimetre wavelengths and upper limits on HCl and H₂O₂. Astron. Astrophys. 521, 5 id.L49.

Hunten, D.M., McElroy, M.B., 1970. Production and escape of hydrogen on Mars. J. Geophys. Res. Space Phys. 75, 5989–6001.

Jain, S.K., Bhardwaj, A., 2011. Model calculations of the N₂ Vegard–Kaplan band emission in Martian dayglow. J. Geophys. Res. 116, E07005. doi:10.1029/2010JE003778.

Jain, S.K., Bhardwaj, A., 2012. Impact of solar EUV flux on CO Cameron band and CO₂⁺ UV doublet emissions in the dayglow of Mars. Planet. Space Sci. 63-64, 110–122. doi:10.1016/j.pss.2011.08.010.

Korablev, O., Bertaux, J.L., Fedorova, A., Fonteyn, D., Stepanov, A., Kalinnikov, Y., Kiselev, A., Grigoriev, A., Jegoulev, V., Perrier, S., Dimarellis, E., Dubois, J.P., Reberac, A., Van Ransbeeck, E., Gondet, B., Montmessin, F., Rodin, A., 2006a. SPICAM IR acousto-optic spectrometer experiment on Mars Express. J. Geophys. Res. 111. doi:10.1029/2006JE002696.

Korablev, O., Bertaux, J., Kalinnikov, Y., Fedorova, A., Moroz, V., Kiselev, A., Stepanov, A., Grigoriev, A., Zhegulev, V., Rodin, A., Dimarellis, E., Dubois, J., Reberac, A., Van Ransbeeck, E., Gondet, B., 2006b. Exploration of Mars in SPICAM-IR experiment onboard the Mars-Express spacecraft: 1. Acousto-optic spectrometer SPICAM-IR. Cosm. Res. 44, 278–293.

Korablev, O., Fedorova, A., Villard, E., Joly, L., Kiselev, A., Belyaev, D., Bertaux, J.-L., 2013. Characterization of the stray light in a space borne atmospheric AOTF spectrometer. Opt. Express 21, 18354.

Krasnopolsky, V., 2002. Far ultraviolet spectrum of Mars. Icarus 160, 86–94. doi:10.1006/icar.2002.6949.

Mahaffy, P.R., Webster, C.R., Atreya, S.K., Franz, H., Wong, M., Conrad, P.G., Harpold, D., Jones, J.J., Leshin, L.A., Manning, H., et al., 2013. Abundance and isotopic composition of gases in the Martian atmosphere from the curiosity rover. Science 341, 263–266.

Krasnopolsky, V.A., 2005. A sensitive search for SO$_2$ in the martian atmosphere: implications for seepage and origin of methane. Icarus 178, 487–492. doi:10.1016/j.icarus.2005.05.006.

Krasnopolsky, V.A., 2006. A sensitive search for nitric oxide in the lower atmospheres of Venus and Mars: detection on Venus and upper limit for Mars. Icarus 182, 80–91. doi:10.1016/j.icarus.2005.12.003.

Leblanc, F., Chaufray, J.Y., Lilensten, J., Witasse, O., Bertaux, J.-L., 2006a. Martian dayglow as seen by the SPICAM UV spectrograph on Mars Express. J. Geophys. Res. 111, E09S11. doi:10.1029/2005JE002664.

Leblanc, F., Witasse, O., Winningham, J., Brain, D., Lilensten, J., Blelly, P.-L., Frahm, R.A., Halekas, J.S., Bertaux, J.L., 2006b. Origins of the Martian aurora observed by spectroscopy for investigation of characteristics of the atmosphere of Mars (SPICAM) on board Mars Express. J. Geophys. Res. 111, A09313. doi:10.1029/2006JA011763.

Leblanc, F., Chaufray, J.Y., Bertaux, J.L., 2007. On Martian nitrogen dayglow emission observed by SPICAM UV spectrograph/Mars Express. Geophys. Res. Lett. 34, L02206. doi:10.1029/2006GL028437.

Leblanc, F., et al., 2008. Observations of aurorae by SPICAM ultraviolet spectrograph on board Mars Express: simultaneous ASPERA-3 and MARSIS measurements. J. Geophys. Res. 113. doi:10.1029/2008JA013033.

Lebonnois, S., Quémerais, E., Montmessin, F., Lefèvre, F., Perrier, S., Bertaux, J.-L., Forget, F., 2006. Vertical distribution of ozone on Mars as measured by SPICAM/Mars Express using stellar occultations. J. Geophys. Res. 111. doi:10.1029/2005JE002643.

Lefèvre, F., Lebonnois, S., Montmessin, F., Forget, F., 2004. Three-dimensional modeling of ozone on Mars. J. Geophys. Res. (Planets) 109, 7004. doi:10.1029/2004JE002268.

Lefèvre, F., Bertaux, J.-L., Clancy, R.T., Encrenaz, T., Fast, K., Forget, F., Lebonnois, S., Montmessin, F., Perrier, S., 2008. Heterogeneous chemistry in the atmosphere of Mars. Nature 454, 971–975. doi:10.1038/nature07116.

Lemmon, M.~T., 14 colleagues, 2004. Atmospheric imaging results from the Mars exploration rovers: spirit and opportunity. Science 306, 1753–1756.

Lopez-Valverde, M.A., Gonzalez-Galindo, F., Lopez-Puertas, M., 2011. Revisiting the radiative balance of the mesosphere of Mars. In: Forget, F., Millour, E. (Eds.), Proceedings of the Mars Atmosphere: Modelling and Observation. Paris, France, pp. 359–362. [Available at http://www-mars.lmd.jussieu.fr/paris2011/program.html].

Määttänen, A., Listowski, C., Montmessin, F., Maltagliati, L., Reberac, A., Joly, L., Bertaux, J.-L., 2013. A complete climatology of the aerosol vertical distribution on Mars from MEx/SPICAM UV solar occultations. ɪcarus 223, 892–941. doi:10.1016/j.icarus.2012.12.001.

Määttänen, A., Montmessin, F., Gondet, B., Scholten, F., Hoffmann, H., González-Galindo, F., Spiga, A., et al., 2010. Mapping the mesospheric CO$_2$ clouds on Mars: MEx/OMEGA and MEx/HRSC observations and challenges for atmospheric models. Icarus 209 (October), 452–469. doi:10.1016/j.icarus.2010.05.017.

Madeleine, J.-B., Forget, F., Millour, E., Montabone, L., Wolff, M.J., 2011. Revisiting the radiative impact of dust on Mars using the LMD global climate model. J. Geophys. Res. (Planets) 116, E11010. doi:10.1029/2011JE003855.

Madeleine, J.-B., Forget, F., Millour, E., Navarro, T., Spiga, A., 2012. The influence of radiatively active water ice clouds on the Martian climate. Geophys. Res. Lett. 39 (661), L23202. doi:10.1029/2012GL053564.

Maltagliati, L., Montmessin, F., Fedorova, A., Korablev, O., Forget, F., Bertaux, J.-L., 2011. Evidence of water vapor in excess of saturation in the atmosphere of Mars. Science 333, 1868. doi:10.1126/science.1207957.

Maltagliati, L., Montmessin, F., Korablev, O., Fedorova, A., Forget, F., Määttänen, A., Lefèvre, F., Bertaux, J.-L., 2013. Annual survey of water vapor vertical distribution and water-aerosol coupling in the Martian atmosphere observed by SPICAM/MEx solar occultations. Icarus 223, 942–962. doi:10.1016/j.icarus.2012.12.012.

Marcq, E., Belyaev, D., Montmessin, F., Fedorova, A., Bertaux, J.-L., Vandaele, A.C., Neefs, E., 2011. An investigation of the SO$_2$ content of the Venusian mesosphere using SPICAV-UV in nadir mode. Icarus 211, 58–69. doi:10.1016/j.icarus.2010.08.021.

Marcq, E., Bertaux, J.-L., Montmessin, F., Belyaev, D., 2013. Variations of sulphur dioxide at the cloud top of Venus's dynamic atmosphere. Nat. Geosci. 6, 25–28. doi:10.1038/ngeo1650.

Mateshvili, N., Fussen, D., Vanhellemont, F., Bingen, C., Dekemper, E., Loodts, N., Tetard, C., 2008. Water ice clouds in the Martian atmosphere: two Martian years of SPICAM nadir UV measurements. Planet. Space Sci. doi:10.1016/j.pss.2008.10.007.

Mateshvili, N., Fussen, D., Vanhellemont, F., Bingen, C., Dodion, J., Montmessin, F., Perrier, S., Dimarellis, E., Bertaux, J.-L., 2006. Martian ice cloud distribution obtained from SPICAM nadir UV measurements. J. Geophys. Res (Planets) 112. doi:10.1029/2006JE002827.

Mateshvili, N., Fussen, D., Vanhellemont, F., Bingen, C., Dodion, J., Montmessin, F., Perrier, S., Bertaux, J.L., 2007. Detection of Martian dust clouds by SPICAM UV nadir measurements during the October 2005 regional dust storm. Adv. Space Res. 40 (6), 869–880. doi:10.1016/j.asr.2007.06.028.

McDunn, T.L., Bougher, S.W., Murphy, J., Smith, M.D., Forget, F., Bertaux, J.-L., Montmessin, F., 2010. Simulating the density and thermal structure of the middle atmosphere (∼80-130 km) of Mars using the MGCM-MTGCM: a comparison with MEX/SPICAM observations. Icarus 206, 5–17. doi:10.1016/j.icarus.2009.06.034.

McElroy, M.B., 1972. Mars: an evolving atmosphere. Science 175, 443.

Montmessin, F., Forget, F., Rannou, P., Cabane, M., Haberle, R.M., 2004. Origin and role of water ice clouds in the Martian water cycle as inferred from a general circulation model. J. Geophy. Res. (Planets) 109, 10004. doi:10.1029/2004JE002284.

Montmessin, F., Quémerais, E., Bertaux, J.L., Korablev, O., Rannou, P., Lebonnois, S., 2006a. Stellar occultations at UV wavelengths by the SPICAM instrument: retrieval and analysis of Martian haze profiles. J. Geophys. Res. (Planets) 111, 9. doi:10.1029/2005JE002662.

Montmessin, F., et al., 2006b. Subvisible CO$_2$ ice clouds detected in the mesosphere of Mars. Icarus 183, 403–410.

Montmessin, F., Lefèvre, F., 2013. Transport-driven formation of a polar ozone layer on Mars. Nat. Geosci. 6, 930–933. doi:10.1038/ngeo1957.

Montmessin, F., Gondet, B., Bibring, J.-P., Langevin, Y., Drossart, P., Forget, F., Fouchet, T., 2007. Hyperspectral imaging of convective CO$_2$ ice clouds in the equatorial mesosphere of Mars. J. Geophys. Res. (Planets) 112, 11.

Montmessin, F., Smith, M.D., Langevin, Y., Mellon, M., Fedorova, A., 2017. The water cycle. In: Haberle, R.M., Todd, C.R., Forget, F., Smith, M.D., Zurek, R.W. (Eds.), The atmosphere and climate of mars. Cambridge University Press, p. 338. ISBN: 978-1-107-01618-7.

Nagy, A.F., Cravens, T.E., 1988. Hot oxygen atoms in the upper atmospheres of Venus and Mars. Geophys. Res. Lett. 15, 433.

Nagy, AndrewF., Gombosi, TamasI., Szego, Karoly, Sagdeev, R.Z., Shapiro, V.D., Shevchenko, V.I., 1990. Venus mantle-Mars planetosphere: what are the similarities and differences? Geophys. Res. Lett. 17 (6), 865–868. doi:10.1029/GL017i006p00865.

Nair, H., Allen, M., Anbar, A.D., Yung, Y., Clancy, R.T., 1994. A photochemical model of the Martian atmosphere. Icarus 111, 124–150. doi:10.1006/icar.1994.1137.

Nakagawa, H., Kasaba, Y., Maezawa, H., Hashimoto, A., Sagawa, H., Murata, I., Okano, S., Aoki, S., Moribe, N., Mizuno, A., Momose, M., Ohnishi, T., Mizuno, N., Nagahama, T., 2009. Search of SO$_2$ in the Martian atmosphere by ground-based submillimeter observation. Planet. Space Sci. 57, 2123–2127. doi:10.1016/j.pss.2009.10.001.

Navarro, T., Madeleine, J.-B, Forget, F., Spiga, A., Millour, E., Montmessin, F., Määttänen, A., 2014. Global climate modeling of the Martian water cycle with improved microphysics and radiatively active water ice clouds. J. Geophys. Res. (Planets) 119. doi:10.1002/2013JE004550.

Owen, T., Biemann, K., Biller, J.E., Lafleur, A.L., Rushneck, D.R., Howarth, D.W., 1977. The composition of the atmosphere at the surface of Mars. J. Geophys. Res. 82, 4635–4639.

Nier, A.O., McElroy, M.B., 1977. Composition and structure of Mars' upper atmosphere - results from the neutral mass spectrometers on Viking 1 and 2. J. Geophys. Res. 82, 4341–4349.

Pang, K., Ajello, J.M., 1977. Complex refractive index of Martian dust – wavelength dependence and composition. Icarus 30, 63–74.

Perrier, S., Bertaux, J.L., Lefèvre, F., Lebonnois, S., Korablev, O., Fedorova, A., Montmessin, F., 2006. Global distribution of total ozone on Mars from SPICAM/MEX UV measurements. J. Geophys. Res. (Planets) 111, 9. doi:10.1029/2006JE002681.

Piccialli, A., Montmessin, F., Belyaev, D., Mahieux, A., Fedorova, A., Marcq, E., Bertaux, J.-L., Tellmann, S., Vandaele, A.C., Korablev, O., 2015. Thermal structure of Venus nightside upper atmosphere measured by stellar occultations with SPICAV/Venus Express. Planet. Space Sci. 321–335. doi:10.1016/j.pss.2014.12.009, 113-11.

Quémerais, E., Bertaux, J.-L., Korablev, O., Dimarellis, E., Cot, C., Sandel, B.R., Fussen, D., 2006. Stellar occultations observed by SPICAM on Mars Express. J. Geophys. Res. (Planets) 111. doi:10.1029/2005JE002604.

Royer, E., Montmessin, F., Bertaux, J.-L., 2010. NO emissions as observed by SPICAV during stellar occultations. Planet. Space Sci. 58, 1314–1326. doi:10.1016/j.pss.2010.05.015.

Sandel, B.R., Groller, H., Yelle, R.V., Koskinen, T., Lewis, N.K, Bertaux, J.-L., Montmessin, F., Quemerais, E., 2015. Altitude profiles of O$_2$ on Mars from SPICAM stellar occultations. Icarus in press).

Schneider, N.M., Deighan, J.I., Jain, S.K., Stiepen, A., Stewart, A.I.F., Larson, D., Mitchell, D.L., Mazelle, C., Lee, C.O., Lillis, R.J., Evans, J.S., Brain, D., Stevens, M.H., McClintock, W.E., Chaffin, M.S., Crismani, M., Holsclaw, G.M., Lefèvre, F., Lo, D.Y., Clarke, J.T., Montmessin, F., Jakosky, B.M., 2015. Discovery of diffuse aurora on Mars. Science 350. doi:10.1126/science.aad0313. aad0313-aad0313

Richardson, M.I., Wilson, R.J., 2002. Investigation of the nature and stability of the Martian seasonal water cycle with a general circulation model. JGR 107. doi:10.1029/2001JE001536.

Shematovich, V.I., Bisikalo, D.V., Gérard, J.-C., Cox, C., Bougher, S.W., Leblanc, F., 2008. Monte Carlo model of electron transport for the calculation of Mars dayglow emissions. J. Geophys. Res. (Planets) 113, E02011. doi:10.1029/2007JE002938.

Simon, C., Witasse, O., Leblanc, F., Gronoff, G., Bertaux, J.-L., 2009. Dayglow on Mars: kinetic modelling with SPICAM UV limb data. Planet. Space Sci. doi:10.1016/j. pss.2008.08.012.

Smith, M.D., 2009. THEMIS observations of Mars aerosol optical depth from 2002–2008. Icarus 202 (2), 444–452.

Smith, M.D., 2004. Interannual variability in TES atmospheric observations of Mars during 1999–2003. Icarus 167, 148–165.

Snow, M., Reberac, A., Quémerais, E., Clarke, J., McClintock, W.E., Woods, T.N., 2013. A new catalog of ultraviolet stellar spectra for calibration. In: Quémerais, E., Snow, M., Bonnet, R.-M. (Eds.), Cross-Calibration of Far UV Spectra of Solar System Objects and the Heliosphere. Springer, New York, NY, p. 191.

Soret, L., Gérard, J.-C., Libert, L., Shematovich, V.I., Bisikalo, D.V., Stiepen, A., Bertaux, J.-L., 2016. SPICAM observations and modeling of Mars aurorae. Icarus 264, 398–406. doi:10.1016/j.icarus.2015.09.023.

Stewart, A.I.F, Alexander, M.J., Meier, R.R., Paxton, L.J., Bougher, S.W., Fesen, C.G., 1992. Atomic oxygen in the Martian thermosphere. J. Geophys. Res. (Planets) 97, 91.

Stiepen, A., Gérard, J.-C., Bougher, S., Montmessin, F., Hubert, B., Bertaux, J.-L., 2015a. Mars thermospheric scale height: CO Cameron and CO_2^+ dayglow observations from Mars Express. Icarus 245, 295–305.

Stiepen, A., Gérard, J.-C., Gagné, M., Montmessin, F., Bertaux, J.-L., 2015b. Ten years of Martian nitric oxide nightglow observations. Geophys. Res. Lett. 42, 720–725. doi:10.1002/2014GL062300.

Strickland, D.J., Stewart, A.I., Barth, C.A., Hord, C.W., 1973. Mariner 9 ultraviolet spectrometer experiment: Mars atomic oxygen 1304 A emission. J. Geophys. Res. (Planets) 78, 4547.

Strickland, D.J., Thomas, G.E., Sparks, P.R., 1972. Mariner 6 and 7 ultraviolet spectrometer experiment: analysis of the O I 1304 and 1356 A emissions. J. Geophys. Res. (Planets) 77, 4052.

Trokhimovskiy, A., Fedorova, A., Korablev, O., Montmessin, F., Bertaux, J.-L., Rodin, A., Smith, M.D., 2015. Mars' water vapor mapping by the SPICAM IR spectrometer: five Martian years of observations. Icarus 251, 50–64.

Tschimmel, M., Ignatiev, N.I., Titov, D.V., Lellouch, E., Fouchet, T., Giuranna, M., Formisano, V., 2008. Investigation of water vapor on Mars with PFS/SW of Mars Express. ıcarus 195, 557–575. doi:10.1016/j.icarus.2008.01.018.

Valeille, A., Tenishev, V., Bougher, S.W., Combi, M.R., Nagy, A., 2009a. Three-dimensional study of Mars upper thermosphere/ionosphere and hot oxygen coronae: 1. General description and results at equinox for low solar conditions. J. Geophys. Res. 114, E11005. doi:10.1029/2009JE003388.

Willame, Y., Vandaele, A.C., Depiesse, C., Lefèvre, F., Letocart, V., Gillotay, D., Montmessin, F., 2017. Retrieving cloud, dust and ozone abundances in the Martian atmosphere using SPICAM/UV nadir spectra. Planer. Space Sci. 142, 9–25. doi:10.1016/j.pss.2017.04.011.

Withers, P., Pratt, R., 2013. An observational study of the response of the upper atmosphere of Mars to lower atmospheric dust storms. Icarus 225, 378–389.

Withers, P., Pratt, R., Bertaux, J-L., Montmessin, F., 2011. Observations of thermal tides in the middle atmosphere of Mars by the SPICAM instrument. J. Geophys. Res. (Planets) 116, E11005. doi:10.1029/2011JE003847.

Wolff, M.J., Bell, J.F., James, P.B., Clancy, R.T., Lee, S.W., 1999. Hubble space telescope observations of the Martian aphelion cloud belt prior to the Pathfinder mission: seasonal and interannual variations. J. Geophys. Res. (Planets) 104, 9027–9042.

Yagi, M., Leblanc, F., Chaufray, J-Y., Gonzalez-Galindo, F., Hess, S., Modolo, R., 2012. Mars exospheric thermal and non-thermal components: seasonal and local variations. Icarus 221, 682–693. doi:10.1016/j.icarus.2012.07.022.